CFD Design and Analysis of Two-Stage Ejector for High-Altitude Testing of Satellite Thrusters

Hamza Rizwan

(2012-NUST-MS-MECH)

A THESIS

SUBMITTED IN PARTIAL FULFILLMENT

OF THE REQUIREMENT FOR THE DEGREE OF

MASTER IN SCIENCE

In

DEPARTMENT OF ENGINEERING SCIENCES

PAKISTAN NAVY ENGINEERING COLLEGE- PNS JAUHAR

NATIONAL UNIVERSITY OF SCIENCE AND TECHNOLOGY

KARACHI PAKISTAN

(2015)

Table of contents

Nomenclature

AR	Area Ratio
ER	Entrainment Ratio
HAT	High Altitude Test Facility
STED	Second Throat Exhaust Diffuser
CFD	Computational Fluid Dynamics
CR	Compression Ratio
ρ	Density
m	Mass
V	Volume
P	Pressure
h	Enthalpy
R	Gas constant with the unit J/(kg.K)
$\overline{R}$	Universal gas constant
W	Molecular weight with unit of kg/(kmol)
M	Mach number
c	Local sound speed
T	Temperature
NASA	National Aeronautics and Space Administration
η	Isentropic Efficiency
A	Area
ω	Entrainment Ratio

γ	Specific heat ratio
ESDU	Engineering Science Data Unit
RANS	Reynolds-averaged Navier-Stokes
K	Kinetic energy
RSM	Reynold's Stress Models
RST	Reynold's Stress Transport
SRS	Scale-resolving simulation
LES	Large eddy simulation
SGS	Sub grid-scale
ν_t	Sub-grid-scale turbulent viscosity
DES	Detached eddy simulation
DNS	Direct Numerical Simulation

Acknowledgement

I would like to thank Prof. Dr. M. Nauman Qureshi and Prof. Dr Shafiqur Rahman for their immense support and positive criticism.

Abstract

This study deals with the design and CFD analysis of a two-stage ejector setup for a High Altitude Simulation for satellite thrusters. To be able to test and evaluate these thrusters, a diffuser-ejectors type experimental setup will be designed using analytical tools/method for the equivalent cold flow configuration. This design will be evaluated and analyzed through numerical modeling and simulations. Steady-state simulations will be run considering the working fluid as perfect gas. The mixing chambers of the ejectors are designed with the assumption that the inner walls are adiabatic and that the primary and secondary streams are uniformly and fully mixed at the end of the chamber. Modeling and meshing of the system will be performed in ANSYS ICEM CFD and solutions have been obtained on CFD solver ANSYS Fluent.

Keywords: CFD, Ejectors, High Altitude Simulation, Thrusters, ANSYS, ICEM, Fluent

1. INTRODUCTION

The space race was one of the most important eras during which an immense amount of research was done and there was no shortage of funds for that research. Both superpowers of that time did all that they could to reach space before the other one. The level of research done during that time on the development of rockets, space shuttles, satellites and on ground test facilities, experimental or theoretical, build the foundation on which most of today's work is based and most of the values that are employed in the current Computational Fluid Dynamics(CFD) software's available today. However, today the picture is quite different. Governments that were initially involved in this space race are cutting back and diverting funds from this field to other promising contenders. Other smaller countries that still come under the developing nations tag are also catching up in this field. These factors have forced scientists and engineers to look into methods that cost less to test and provide results as accurate as or even better than those employed previously. Testing thrusters on the ground requires specialized testing facilities called High Altitude Test Facilities or HAT for short, that can simulate the conditions of outer space namely the vacuum levels found in space. To achieve this different designs of testing facilities are employed which range from simple second throat exhaust diffusers (STED) to combinations using vacuum pumps and/or gas ejectors in series with the diffusers to achieve better results. As far as the scope of this paper goes it focuses on the subject of CFD with derivations from equations relating to gas dynamics.

This thesis attempts on studying a model of a HAT provided by SUPARCO which is Pakistan's Space Agency. The model consists of a STED which has been coupled with a two stage ejector system to provide better vacuum conditions and hence achieve better results while testing thrusters. The initial mass flow rates provided by SUPARCO were used to test this model. An initial run was done FLUENT to verify if the thruster start up pressure and consequently further simulations followed to finalize the results and reach a conclusion regarding the provided model.

1.1 Objective

As discussed above the aerospace industry is limited currently in terms of funding and that is especially true in Pakistan. With that in mind the objective of this study was to perform an analysis and optimize the design of a HAT.

1.2 Organization of Thesis:

This thesis is comprised of three major portions. The first is a case study along with a brief literature review which serves as an introduction to some of the basic laws of gas dynamics including workings on the flow through a nozzle. Ample knowledge has been shared in this part to provide the reader a basic understanding of the scope of this thesis and some of the concepts that form the base of this work. Also included in this section are the applications and comparisons of different HAT setups which have been extracted from previous studies along with their references. This part includes a complete introduction and a run-through of a HAT detailing different components and combinations along with their distinct advantages and disadvantages. A concise schematic diagram of the HAT being used for this thesis is also included within this section to give the reader a broad overview of the schematic before diving the calculations. The second part solely focuses on the methodology of this thesis. It contains comparisons of turbulence models, the design of the HAT and its subsequent meshing. This part also gives a brief working of the constant area model optimization method that was used to come up with the dimensions of the HAT. The final section will demonstrate the results of the simulations performed, results have been presented with their corresponding graphical representation. Contour plots have been added to give a visual representation of what is happening inside the test chamber during the starting up of the thruster.

1.3 Theoretical Background

1.3.1 Gas Dynamics - Introduction

The theoretical background used in the derivation of 1-D analytical models for gas ejectors is introduced in this chapter. All 1-D analysis of compressible gas streams in the ejector are made by application of the equations of the conservation of momentum, continuity and energy, as well as the ideal-gas law. The Mach number is an effective dimensionless parameter to represent the velocity, and is hence employed for compressible flow. Isentropic expansion is an important assumption during the derivations, though some researchers also use loss factor coefficients obtained from experimental data to represent the friction or other loss. For performance that is optimal, gas ejectors in the modern day are typically operated within supersonic conditions at the primary nozzle's exit point. Therefore, it is necessary to introduce the choking phenomena occurs at the throat of primary nozzle. The basic idea of a gas ejector is to accelerate the motive flow to supersonic by a converging-diverging nozzle, primary flow exit at the suction chamber where secondary flow is induced by this high-velocity, depressurized flow. In most cases, there is also a diffuser installed at the exit of the mixing section to induce pressure recovery.

1.3.1.1 Conservation and Ideal Gas Law

The conservation equations and idea gas law for steady 1-D compressible flow in an arbitrary variable-area control volume as sketched in Fig.1 are given below. The definitions of terminologies can be found in the nomenclature section.

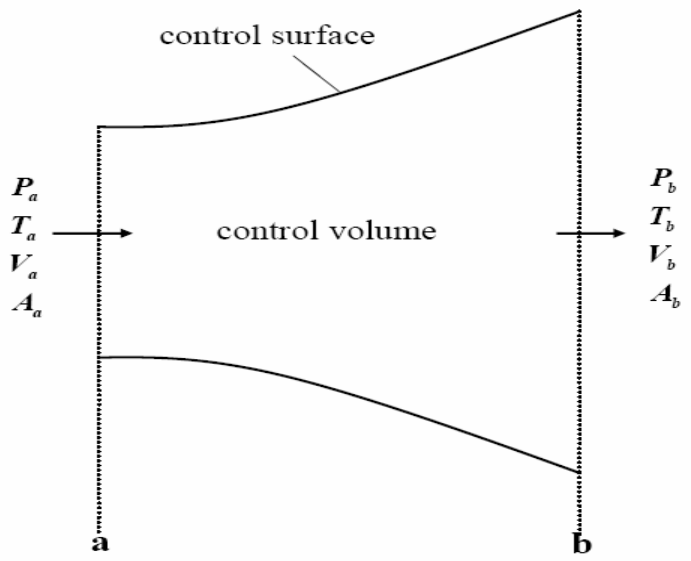

Fig. 1: Control volume for 1-D flow

Continuity equation

$$m = \rho_a V_a A_a = \rho_b V_b A_b$$

Momentum equation

$$PA_a + mV_a + \int_{A_a}^{A_b} PdA = mV_b + PA_b$$

Energy equation

$$h_a + \frac{{V_a}^2}{2} = h_b + \frac{{V_b}^2}{2}$$

Ideal gas law

$$\frac{P}{\rho} = RT$$

Where the gas constant is denoted by R with unit of J/(kg.K). R relates to its molecular weight by the following equation:

$$R = \frac{\bar{R}}{W}$$

In the above equation, $\bar{R}$ is the universal gas constant with unit of J/(kmol.K) and

the molecular weight is denoted as W with unit of kg/(kmol) .

1.3.1.2 Mach Number

Compressible flow, and particularly supersonic flow, are values best represented by the Mach number, denoted by M. A dimensionless parameter, which is defined as the ratio of the fluid velocity to the local sonic speed, is known as the Mach number.

$$M = \frac{Local\ Fluid\ Velocity}{Local\ Sonic\ Speed} = \frac{V}{c}$$

The local sound speed c in a medium with temperature T is given by:

$$c = \sqrt{\gamma RT}$$

1.3.1.3 Choking Phenomena

To explain the choking phenomena, a convergent-divergent nozzle with its static pressure distribution along the flow direction are shown in Fig.2. Flow through the Converging-diverging nozzle of Fig. 2 is induced by an adjustable lower downstream pressure; upstream supply is constant and stagnation conditions with $V_0 \cong 0$. P_e and P_b represent the static pressure in the nozzle exit plane and the back pressure, respectively. Fig 2 illustrates graphically the effect of variations in the back pressure P_b on the pressure distribution through the nozzle. The flow rate is low when back pressure P_b is slightly less than P_0 ; curve i shows the pressure distribution in the nozzle for this case. If the flow rate is low enough, the flow will be subsonic and essentially incompressible (if M < 0.3) at all points on this curve. Under this condition, the nozzle will behave as a venturi, with flow accelerating in the converging portion until a point of maximum velocity and minimum pressure is reached at the throat, then decelerating in the diverging portion to the nozzle exit. When the back

pressure is reduced further, the flow rate increases but, is still subsonic everywhere and the pressure distribution is shown as curve *ii* similar to curve *i* although the compressibility effects become important. As P_b continues to be reduced, the flow rate will continue to increase.

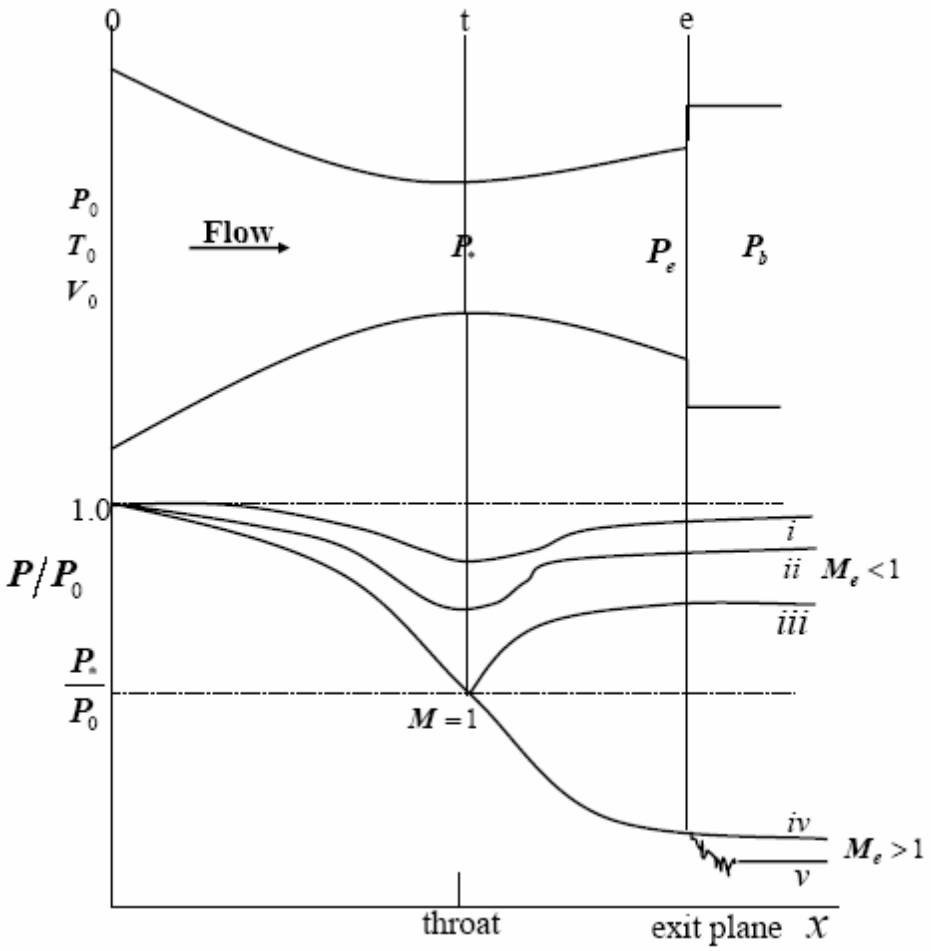

Fig. 2: Pressure profile for isentropic flow in a converging-diverging nozzle

If back pressure P_b is lowered far enough, ultimately the flow reaches M =1 at nozzle throat—the section of minimum flow area, as shown on curve *iii* and the nozzle is choked. When curve *iii* is reached, critical conditions are present at the throat and the mass flow rate attains the maximum possible for the given nozzle and stagnation conditions. The corresponding pressure is the critical back pressure, P_*. The definition of critical condition is the state at which the Mach number is unity.

1.4 Computational Fluid Dynamics

The Navier-Stokes equation is one of the fundamental governing equations for Newtonian fluid dynamics, and has been known for over 150 years. However, these equations require complex solutions making it difficult to simulate them for better understanding. Computational Fluid Dynamics (CFD) bypasses the complexity of traditional methods by developing numerical solutions to these governing equations. The solution is significantly cost-effective, and allows for a sharper analysis than currently provided. That being said, there is still a significant amount of active research being conducted in order to identify these equations in their reduced forms. One such area is the turbulent closure Reynolds-averaged Navier Stokes equations.

These experimental methods allow for a pre-testing phase and act as an important tool for validating the approximations to governing equations. Not only does this offer an economical alternative to full-scale testing, it also allows us to explore the limits of these governing equations, particularly wind tunnel and rig tests.

1.4.1 Applications of Computational Fluid Dynamics

The applications of CFD are immense. They can range from anywhere from a simple simulation of a flow around an airfoil to complicated flows through human veins and arteries. In this section we will go over a few of these applications. Commercial CFD packages that are available can be used to perform all of the above mentioned simulations with a high level of accuracy. Shown below is an example of the applications of CFD in the aerospace industry.

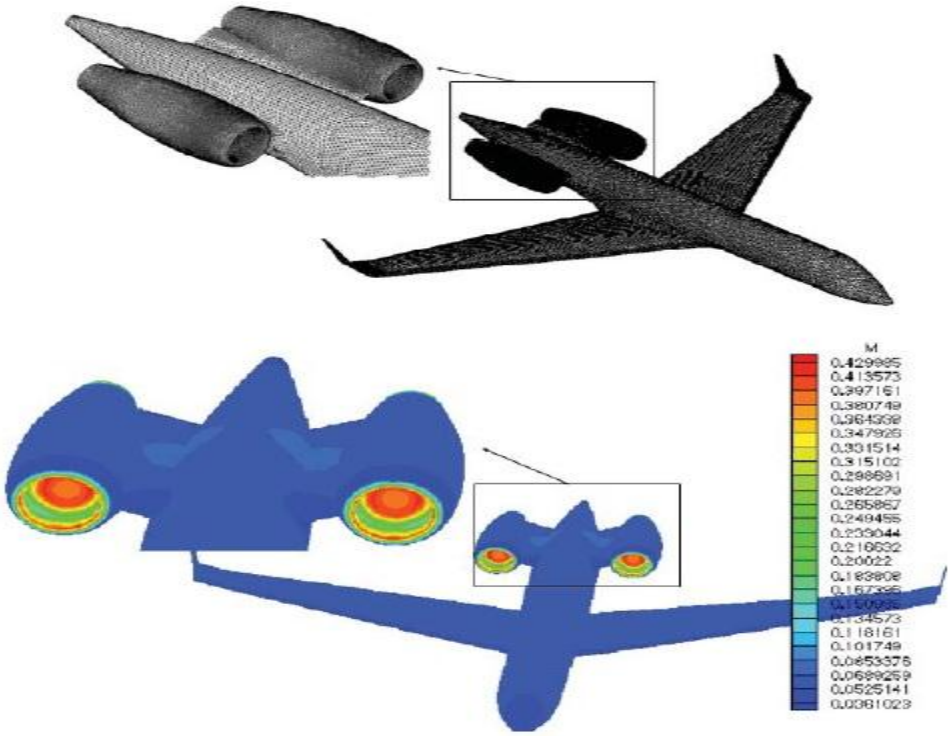

Fig. 3: Grid and flow solution for a civil aircraft with nacelles

This is an example of a flow around this aircraft. It can also be a modeled to simulate the flow through the engines with complete primary flow paths through the turbine and compressor blades included as well as secondary flow paths through cooling cavities, bleeds, around seals and also through intake ducts. Another example which has also become one of the major applications of CFD is the bio-medical field. These simulations are mostly done for the two phase or three phase interactions between medicines and blood. This modeling of the arteries and blood flow through them is known as Blood Rheology and has very important applications in the design of drug delivery systems. Fig. 4 shows a simulation being run to observe the flow through an inhaler

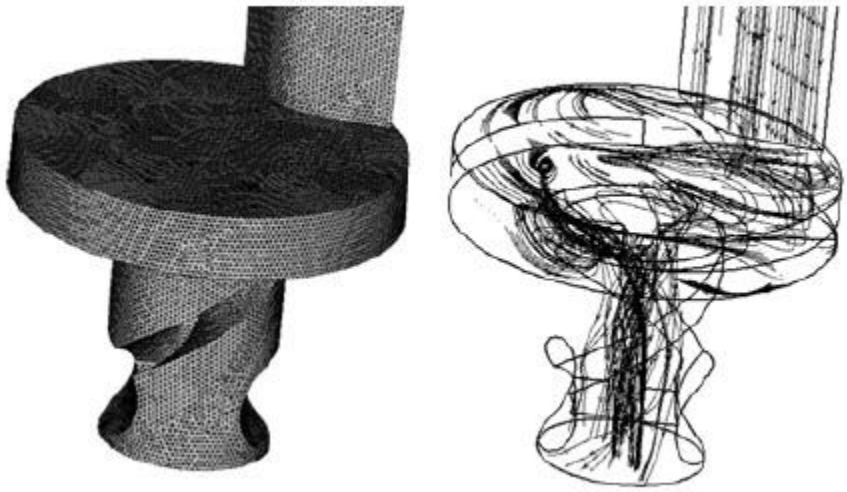

Fig. 4: Grid and flow inside an inhaler

CFD is a low cost alternative to physical testing. Due to this reason it is of more interest to industries that are directly or indirectly related to thermal fluid engineering experimentation. However, as a side-note, complex flow simulations are challenging and may not provide correct results and it takes a lot of technical proficiency to obtain validated results.

2. LITERATURE REVIEW

Rocket engines that are designed to operate in the upper atmosphere or in space require an appropriate setup to test their performance and efficiency on the ground. Since they require very low pressures to operate and testing them requires a setup that replicates those conditions. Satellite thrusters are meant to operate in vacuum, hence these employ large area ratio nozzles (AR≥100). If these thrusters are tested at ground without appropriate auxiliaries, the nozzle becomes over-expanded and separation occurs in the nozzle divergent section. This makes the on-ground testing and performance evaluation of thrusters impossible.

Up until now experimental investigations regarding this setup have been performed in great detail. NASA in its experimental investigation (Massier & Roschke, 1960) found three optimum diffuser geometries that were practical and gave convincing results. They focused on a second throat configuration with a slight offset in the nozzle exit diameter and diffuser inlet. This was done in order to use the momentum of the exhaust nozzle gases to create a vacuum.

This study involves a combination setup with a two stage ejector attached to the diffuser exit. This configuration is employed in order to achieve the desired vacuum in the test facility. Since the thruster operates in a very low pressure environment (~3 mbar) and produces a thrust of about 20N at full-flow conditions. Since this is a very low momentum the diffuser action will not be noticeable. A single diffuser ejector configuration cannot achieve the given conditions and due to this fact we employ a two stage ejector to get the desired conditions. The ejector is operated before the thruster is ignited to achieve the low pressure conditions inside the test facility. The creation of low vacuum using the external ejector system is reported elsewhere [Manikanda Kumaran et al., October 2009].

In the current study a constant vacuum (~3 mbar) will be assumed throughout the facility. The exhaust diffuser will be designed according to one of the configurations used by Massier & Roschke, 1960. The two stage ejector will then be modeled accordingly.

3. GAS EJECTOR 1-D ANALYTICAL MODELS

3.1. Introduction

This chapter focuses on 1-D analytical models for analyzing the design and performance of ejectors with single phase gas flow. Each section of the ejector will undergo a detailed analysis including: the mixing chamber, supersonic primary nozzle, and the second throat exhaust diffuser. The flow model for the mixing chamber is the key issue for ejector design. The two widely adopted ejector mixing models are the constant-area and constant-pressure mixing models [19, 17]. Equations of analytical models for the primary and secondary streams are derived in extensive detail, ensuring that they incorporate varying working gases across a range of molecular weights and thermodynamic properties to give a representative sample.

The merits and problems of 1-D analytical models will be summarized and discussed. Gas ejector design can be implemented by employing equations of constant-area mixing approach.

3.2. Supersonic Primary Nozzle

Fig. 5 shows the standard components used within a gas ejector. Primary focus is on a typical supersonic primary nozzle. The nozzle's inlet, throat, and sections represented by 0, t and 1, respectively are the exit section. The supersonic primary nozzle has been mentioned in the previous chapter, and Equation (2.17) and Equation (2.21) were derived to calculate the maximum mass flow rate and the ratio of the areas of nozzle exit to throat. However, those equations were derived based on the assumption of isentropic expansion in the primary nozzle. In actual situations, ejectors and their downstream pressures are seldom operated according to The unique design conditions of the nozzle geometry. Doing so causes shock waves to occur outside the nozzle in the form of irreversible over or under-expansion. To account for this phenomenon, it is imperative to introduce a coefficient which represents the isentropic efficiency of compressible flow. Denoted by η_n, it accounts for any anomalous expansion, particularly divergent, in the compressible flow at the nozzle.

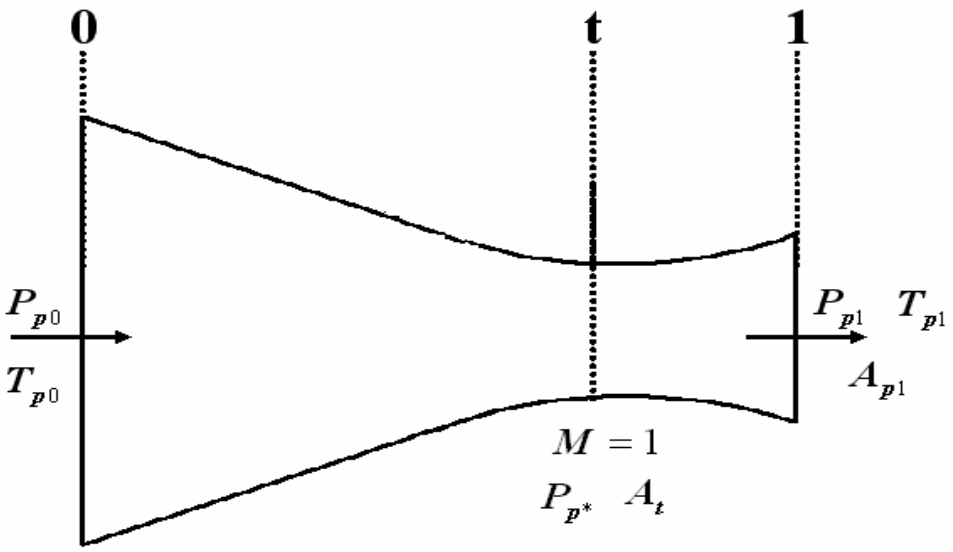

Fig. 5: Supersonic Primary Nozzle

The isentropic assumption is applied for the converging part. The isentropic assumption For the converging section through the nozzle's throat, is still used. Flow parameters: P_{p^*}, T_{p^*}, ρ_{p^*} and V_{p^*} at the nozzle throat can be calculated by using Equations (2.12), (2.13), (2.14) and (2.15). According to Equation (2.17), the mass flow rate of the primary stream is

$$\boldsymbol{m_p} = \frac{\boldsymbol{A_t P_0}}{\sqrt{\boldsymbol{T_0}}} \sqrt{\frac{\boldsymbol{\gamma_p}}{\boldsymbol{R_p}} \left(\frac{\boldsymbol{2}}{\boldsymbol{\gamma_p + 1}}\right)^{\frac{\boldsymbol{\gamma_p + 1}}{\boldsymbol{\gamma_p - 1}}}} \qquad (3.1)$$

For the diverging expansion part of the nozzle, the isentropic efficiency is written as:

$$\eta_n = \frac{h_{p0} - h_{p1}}{h_{p0} - h_{p1s}} \qquad (3.2)$$

where h_{p0} is the primary stream stagnation enthalpy; h_{p1} is the exit enthalpy under the actual working conditions; h_{p1s} is the isentropic enthalpy for the same exit pressure. For the nozzle shown in Fig. 5 we can write the steady flow energy equation as:

$$h_{p0} = h_{p1} + \frac{V_{p1}^2}{2} \tag{3.3}$$

With $h_p = c_p T$, using Equation (3.2) we can obtain Equation (3.4).

$$\frac{T_{p1s}}{T_{p0}} = 1 - \frac{1}{\eta_n}\left(1 - \frac{T_{p1}}{T_{p0}}\right) \tag{3.4}$$

The ratio of stagnation temperature to the static temperature according to the isentropic expansion function is

$$\frac{T_0}{T} = 1 + \frac{\gamma - 1}{2} M^2 \tag{3.5}$$

By using the isentropic relations and working with Equations (3.4), (3.5) the derivation for the primary nozzle pressure ratio is as shown below:

$$\frac{P_{p1}}{P_{p0}} = \left[1 - \frac{1}{\eta_n} + \frac{1}{\eta_n\left(1 + \frac{\gamma_p - 1}{2} M_{p1}^2\right)}\right]^{\frac{\gamma_p}{\gamma_p - 1}} = f_1\left(\gamma_p, M, \eta_n\right) \tag{3.6}$$

The mass flow rate through the nozzle is constant. It is expressed as:

$$m_p = \rho_p A V = PAM\left(\frac{\gamma_p}{R_p T}\right)^{\frac{1}{2}} \tag{3.7}$$

Considering mass conservation, i.e.,$m_{p1} = m_{p*}$ the primary nozzle area ratio of exit to throat becomes

$$\frac{A_{p1}}{A_t} = \frac{P_{p*}}{P_{p1}} \frac{1}{M_{p1}} \left(\frac{T_{p1}}{T_{p*}} \right)^{\frac{1}{2}} \tag{3.8}$$

Equation (3.8) can be rewritten, by substituting from Equation (3.5) and Equation (3.6), as:

$$\frac{A_{p1}}{A_t} = \frac{1}{M_{p1}} \left(\frac{2}{\gamma+1} \right)^{\frac{\gamma_p+1}{2(\gamma_p-1)}} \left[1 - \frac{1}{\eta_n} + \frac{1}{\eta_n \left(1+\frac{\gamma_p-1}{2} M_{p1}^2 \right)} \right]^{\frac{-(\gamma_p+1)}{2(\gamma_p-1)}} \tag{3.9}$$

3.3. Constant-Area Mixing Model

Shown in Fig. 6 is a gas ejector schematic, its design being based on the constant-area mixing model. The location of the exit plane of the primary nozzle is within the constant-area mixing section. The primary and secondary stream start mixing at the inlet and the process completes at the exit of this mixing chamber. The aerodynamic throat as shown in Fig. 6, is an important concept in Fabri's theory [18] and usually can occur in the constant-area mixing chamber during operation. This aerodynamic throat would significantly impact the performance of the ejector. When the static pressure of the primary stream is more than that of the secondary stream in section between 1 and 2, the primary stream expands against secondary stream. Thus, the primary steam creates an artificial throat within the mixing chamber due to its interaction with the secondary stream by behaving like an aerodynamic throat. The secondary stream could be choked at the aerodynamic throat if the downstream pressure is low enough.

In the first part of this section equations will be derived for a constant-area mixing model without an aerodynamic throat occurring in the mixing chamber. The second part of this section will include the aerodynamic throat phenomena.

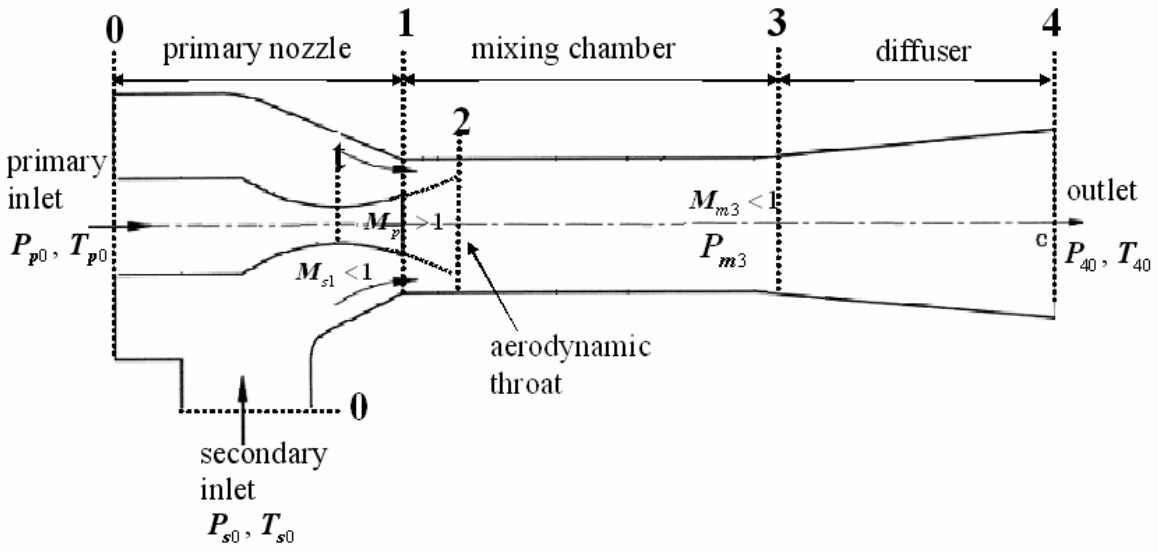

Fig. 6: Constant Area Ejector Schematic

3.3.1 Derivation of Constant-Area Mixing Model without Aerodynamic Throat

Fig. 7 is the control volume selected to analyze the flow in the mixing chamber of a constant-area ejector. Derivation of the constant-area model is based on the following assumptions:

1) Streams are in steady state;
2) All streams – primary and secondary – are fully uniform at section 1, ultimately getting fully mixed at section 3;
3) Both streams behave in a manner which can be considered similar to perfect gases;
4) Sections 1 and 3 are divided by an adiabatic inner wall.

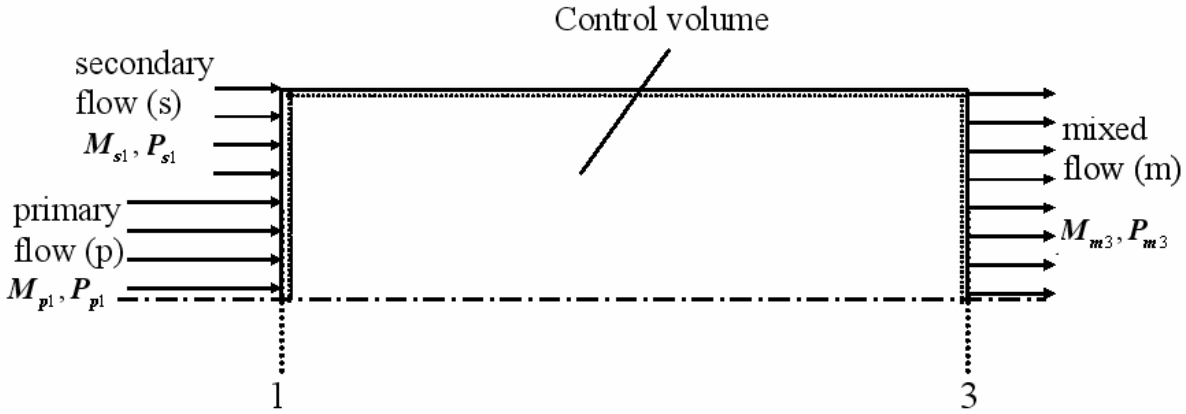

Fig. 7: Control volume for derivation of constant-area mixing model

The entrainment ratio (ER) ω, defined at the inlet of the mixing chamber as the mass flow ratio of the secondary stream to the primary stream,

$$\omega = \frac{m_{s1}}{m_{p1}} = \frac{A_{p1}}{A_{s1}} \frac{P_{p1}}{P_{s1}} \left(\frac{T_{p0}}{T_{s0}}\right)^{\frac{1}{2}} \left(\frac{R_p}{R_s}\right)^{\frac{1}{2}} \frac{f_2(\gamma_s, M_{s1})}{f_2(\gamma_p, M_{p1})} \tag{3.10}$$

Where, $f_2(\gamma, M)$ is the mass flow function,

$$f_2(\gamma, M) = \frac{m}{PA} (RT_0)^{\frac{1}{2}} = M \left[\gamma \left(1 + \frac{\gamma - 1}{2} M^2\right)\right]^{\frac{1}{2}} \tag{3.11}$$

Solving for the static pressure ratio of the secondary to the primary stream at the mixing chamber inlet $\frac{P_{p1}}{P_{s1}}$ from Equation (3.10), the following expression can be obtained:

$$\frac{P_{p1}}{P_{s1}} = \frac{A_{p1}}{A_{s1}} \left(\frac{T_{p0}}{T_{s0}}\right)^{\frac{1}{2}} \left(\frac{R_p}{R_s}\right)^{\frac{1}{2}} \frac{f_2(\gamma_s, M_{s1})}{f_2(\gamma_p, M_{p1})} \omega \tag{3.12}$$

Considering the continuity equation for the control volume in Fig. 7,

$$m_{p1} + m_{s1} = m_{m3} \tag{3.13}$$

As shown in Equation (3.11), the expression for mass flow rate can be written as:

$$m = \frac{PA}{(RT_0)^{\frac{1}{2}}} f_2(\gamma, M) \tag{3.14}$$

An expression can be derived by substituting Equation (3.14) into Equation (3.13), as shown below:

$$\frac{P_{m3}}{P_{p1}} = \frac{A_{p1}}{A_{m3}} \left(\frac{T_{m0}}{T_{p0}}\right)^{\frac{1}{2}} \left(\frac{R_m}{R_p}\right)^{\frac{1}{2}} \frac{f_2(\gamma_p, M_{p1})}{f_2(\gamma_m, M_{m3})} (1+\omega) \tag{3.15}$$

In the above equation, the gas constant R_m and specific heat ratio γ_m of the mixed flow are defined as:

$$R_m = \frac{R_p + \omega R_s}{1+\omega} \tag{3.16}$$

$$\gamma_m = \frac{\frac{\gamma_p}{\gamma_p - 1} + \frac{\gamma_s}{\gamma_s - 1} \frac{R_s}{R_p} \omega}{\frac{1}{\gamma_p - 1} + \frac{1}{\gamma_s - 1} \frac{R_s}{R_p} \omega} \tag{3.17}$$

With the above stated assumptions the energy conservation over the control volume shown in Fig. 7, can be written as:

$$m_p h_{p0} + m_s h_{s0} = m_m h_{m0} \tag{3.18}$$

Using continuity Equation (3.13) and substituting $h_0 = c_p T_0$ into energy Equation (3.18), the stagnation temperature ratio of mixed flow to the primary flow is obtained:

$$\frac{T_{m0}}{T_{p0}} = \frac{\frac{\gamma_p}{\gamma_p - 1} + \frac{\gamma_s}{\gamma_s - 1} \frac{R_s}{R_p} \frac{T_{s0}}{T_{p0}} \omega}{\frac{\gamma_p}{\gamma_p - 1} + \frac{\gamma_s}{\gamma_s - 1} \frac{R_s}{R_p} \omega} \tag{3.19}$$

The stagnation pressure ratio of the secondary stream to the primary steam is

$$\frac{P_{s0}}{P_{p0}} = \frac{P_{s1}}{P_{p1}} \frac{f_1\left(\gamma_p, M_{p1}, \eta_n\right)}{f_3(\gamma_s, M_{s1})} \tag{3.20}$$

Where,

$$f_3(\gamma_s, M) \equiv \frac{P_{s1}}{P_{s0}} = \left(1 + \frac{\gamma_s - 1}{2} {M_{s1}}^2\right)^{\frac{-\gamma_s}{\gamma_s - 1}} \tag{3.21}$$

The momentum conservation equation for the control volume is

$$P_{p1}A_{p1} + P_{s1}A_{s1} + \rho_{p1}A_{p1}V_{p1}^2 + \rho_{s1}A_{s1}V_{s1}^2 = P_{m3}A_{m3} + \rho_{m3}A_{m3}V_{m3}^2 \tag{3.22}$$

According to gas state equation, local gas density can be expressed as:

$$\rho = \frac{P}{RT} \tag{3.23}$$

The local velocity can be expressed as a function of Mach number:

$$V^2 = M^2 \gamma RT \tag{3.24}$$

The momentum conservation can be defined, by substituting Equation (3.23) and Equation (3.24) into Equation (3.22), as:

$$\frac{P_{s1}}{P_{p1}} \frac{A_{s1}}{A_{p1}} (1 + \gamma_s M_{s1}^2) + \left(1 + \gamma_p M_{p1}^2\right) = \frac{P_{m3}}{P_{p1}} \frac{A_{m3}}{A_{p1}} (1 + \gamma_m M_{m3}^2) \tag{3.25}$$

By substituting Equations (3.12) and (3.15) in Equation (3.25) the solution for the Mach number at the mixing chamber exit can be obtained:

$$M_{m3} = \sqrt{\frac{-(\alpha^2 - 2)^2 \pm \sqrt{(\alpha^2 - 2)^2 + 2\left(\frac{\gamma_m - 1}{\gamma_m}\right)\left(\alpha^2 - \frac{2\gamma_m}{\gamma_m - 1}\right)}}{(\gamma_m - 1)\left(\alpha^2 - \frac{2\gamma_m}{\gamma_m - 1}\right)}} \tag{3.26}$$

Where,

$$\alpha = \frac{\left(\frac{T_{s0}}{T_{p0}}\right)^{\frac{1}{2}}\left(\frac{R_s}{R_p}\right)^{\frac{1}{2}} f_4(\gamma_s, M_{s1})w + f_4(\gamma_p, M_{p1})}{\left(\frac{T_{m0}}{T_{p0}}\right)^{\frac{1}{2}}\left(\frac{R_m}{R_p}\right)^{\frac{1}{2}}(1+w)} \tag{3.27}$$

And

$$f_4(\gamma, M) = \frac{1+\gamma M^2}{M}\left[\gamma\left(1 + \frac{\gamma-1}{2}M^2\right)\right]^{\frac{-1}{2}} \tag{3.28}$$

So far, the flow field parameters at the mixing chamber exit are all obtained through the solutions of conservation equations of mass, momentum, and energy over the control volume as shown in Fig. 7. The velocity which is represented by Mach number can be calculated by using Equation (3.26); the static pressure and the stagnation temperature can be calculated by using Equation (3.15) and (3.19), respectively. To calculate these parameters, it may be more convenient to make the entrainment ratio, ω, be a function of the area ratio.

Considering that $A_{s1} = A_{m3+}A_{p1}$ and using Equation (3.9), the area ratio of secondary stream to primary stream at the mixing chamber inlet can be expressed as:

$$\frac{A_{s1}}{A_{p1}} = \frac{A_{m3}}{A_t}\frac{1}{f_5(\gamma_p, M_{p1}, \eta_n)} - 1 \tag{3.29}$$

$f_5(\gamma_p, M_{p1}, \eta_n)$ is defined as

$$f_5(\gamma_p, M_{p1}, \eta_n) = \frac{1}{M_{p1}}\left(\frac{2}{\gamma+1}\right)^{\frac{\gamma_p+1}{2(\gamma_p-1)}}\left[1 - \frac{1}{\eta_n} + \frac{1}{\eta_n\left(1+\frac{\gamma_p-1}{2}M_{p1}^2\right)}\right]^{\frac{-(\gamma_p+1)}{2(\gamma_p-1)}} \tag{3.30}$$

Rearranging Equation (3.20) to give,

$$\frac{P_{s1}}{P_{p1}} = \frac{P_{s0}}{P_{p0}}\frac{f_3(\gamma_s, M_{s1})}{f_1(\gamma_p, M_{p1}, \eta_n)} \tag{3.31}$$

The relationship of ER with area ratio can be derived by substituting Equation (3.29) and

Equation (3.31) into Equation (3.10), according to the definitions of $f_1(\gamma_p, M_{p1}, \eta_n)$, $f_2(\gamma, M)$ and $f_3(\gamma, M)$.

$$\omega = \frac{M_{s1}}{M_{p1}} \frac{A_{p1}}{A_{s1}} \frac{P_{p0}}{P_{s0}} \left(\frac{T_{p0}}{T_{s0}}\right)^{\frac{1}{2}} \left(\frac{R_p}{R_s}\right)^{\frac{1}{2}} \left(\frac{\gamma_s}{\gamma_p}\right)^{\frac{1}{2}} \left(\frac{A_{m3}}{A_t} \frac{1}{f_5(\gamma_p, M_{p1}, \eta_n)} - 1\right) \frac{\left(1+\frac{\gamma_s-1}{2} M_{s1}^2\right)^{\frac{-(\gamma_p+1)}{2(\gamma_p-1)}}}{\left(1+\frac{\gamma_p-1}{2} M_{p1}^2\right)^{\frac{-(\gamma_p+1)}{2(\gamma_p-1)}}} \left[1 + \left(\frac{\eta_n-1}{\eta_n}\right) \frac{\gamma_p-1}{2} M_{p1}^2\right]^{\frac{-\gamma_p}{\gamma_p-1}} \quad (3.32)$$

3.3.2 Derivation of Constant-Area Mixing Model with Aerodynamic Throat

Fig. 8 shows a control volume of the initial interaction region in the constant-area mixing chamber. This control volume was used for derivation of equations for constant area mixing model operating in the supersonic regime (SR). The following prerequisite assumptions are necessary in order to conduct an accurate analysis of the region's flow:

5) There is no mixing of the streams in sections 1 and 2; both streams are isentropic.
6) The secondary stream is choked at section 2, i.e., $M_{s2} = 1$.
7) At the inlet, secondary static pressure is less than that of the primary. i.e., $P_{p1} > P_{s1}$.

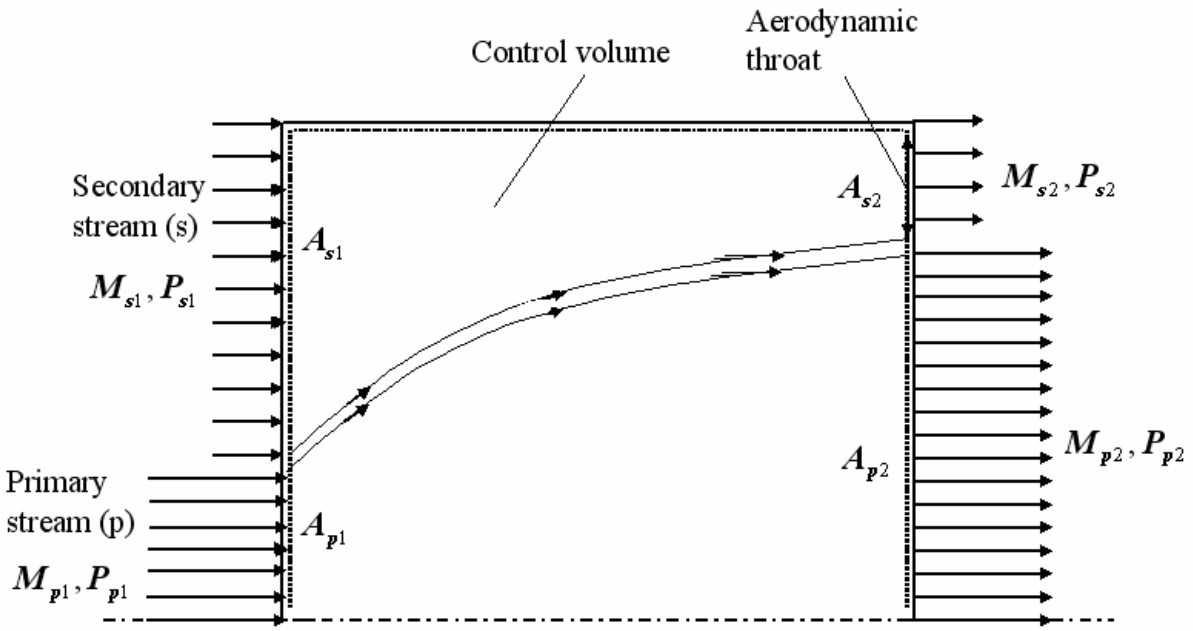

Fig. 8: Control volume for analysis of initial interaction region

The area ratio of primary stream at section 1 to nozzle throat can be derived starting from the following equation:

$$\frac{A_{p2}}{A_t} = \frac{A_{p2}}{A_{p1}} \frac{A_{p1}}{A_t} \tag{3.33}$$

Considering that $A_{p2} = A_{m3} - A_{s2}$ and $A_{s1} = A_{m3} - A_{p1}$ and substituting Equation (3.9) into Equation (3.33), Equation (3.34) is obtained:

$$\frac{A_{p2}}{A_t} = \frac{1-\frac{1-(A_{p1}/A_{m3})}{A_{S1}/A_{S2}}}{A_{p1}/A_{m3}} \frac{1}{M_{p1}} \left(\frac{2}{\gamma+1}\right)^{\frac{\gamma p+1}{2(\gamma p-1)}} \left[1 - \frac{\frac{\gamma p-1}{2} M_{p1}^2}{\eta_n\left(1+\frac{\gamma p-1}{2} M_{p1}^2\right)}\right]^{\frac{-(\gamma p+1)}{2(\gamma p-1)}} \tag{3.34}$$

The above ratio of areas can also be derived, similar to Equation (3.8), in the following form:

$$\frac{A_{p2}}{A_t} = \frac{P_{p*}}{P_{p2}} \frac{1}{M_{p2}} \left[\frac{1+\frac{\gamma_p - 1}{2}}{\left(1+\frac{\gamma_p - 1}{2} M_{p2}^2\right)} \right]^{\frac{1}{2}} \tag{3.35}$$

The $\frac{\mathrm{P_{p*}}}{\mathrm{P_{p2}}}$ in Equation (3.35) can be expressed as:

$$\frac{P_{p*}}{P_{p2}} = \frac{P_{p*}}{P_{p0}} \frac{P_{p0}}{P_{p1}} \frac{P_{p1}}{P_{p2}} = \frac{P_{p*}}{P_{p0}} \Big/ \left(\frac{P_{p2}}{P_{p1}} \frac{P_{p1}}{P_{p0}} \right) \tag{3.36}$$

From Equation (3.5) and the isentropic relations, the equation can be written as

$$\frac{P_{p2}}{P_{p1}} = \left(\frac{1+\frac{\gamma_p - 1}{2} M_{p1}^2}{1+\frac{\gamma_p - 1}{2} M_{p2}^2} \right)^{\frac{\gamma_p}{\gamma_p - 1}} \tag{3.37}$$

$\frac{P_{p*}}{P_{p0}}$ in Equation (3.36) can be derived similarly to Equation (3.6). Substituting the $\frac{P_{p*}}{P_{p0}}$, Equation (3.6) and Equation (3.37) into Equation (3.35), the following expression is obtained:

$$\frac{A_{p2}}{A_t} = \frac{1}{M_{p2}} \left(\frac{2}{\gamma+1} \right)^{\frac{\gamma_p + 1}{2(\gamma_p - 1)}} \left(1 + \frac{\gamma_p - 1}{2} {M_{p2}}^2 \right)^{\frac{-\gamma_{p+1}}{2(\gamma_p - 1)}} \left[1 + \left(\frac{\eta_n - 1}{\eta_n} \right) \frac{\gamma_p - 1}{2} M_{p1}^2 \right]^{\frac{-\gamma_p}{\gamma_p - 1}} \tag{3.38}$$

Thus, M_{p2} can be found by using Equation (3.34) and Equation (3.38).

The momentum equation for the control volume shown in Fig. 8 is

$$P_{p1}A_{p1} + P_{s1}A_{s1} + \rho_{p1}A_{p1}V_{p1}^2 + \rho_{s1}A_{s1}V_{s1}^2 = P_{p2}A_{p2} + P_{s2}A_{s2} + \rho_{p2}A_{p2}V_{p2}^2 + \rho_{s2}A_{s2}V_{s2}^2 \quad (3.39)$$

Considering that $M_{s2} = 1$ and $A_{s1} = A_{m3} - A_{p1}$ from Fig. 8 and also solving for $\frac{P_{s1}}{P_{p1}}$ from Equation (3.39), the inlet static pressure ratio can be obtained as:

$$\frac{P_{s1}}{P_{p1}} = \frac{\left(\frac{P_{p2}/P_{p0}}{P_{p1}/P_{p0}}\right)\left(\frac{A_{p2}/A_{p*}}{A_{p1}/A_{p*}}\right)\left(1+\gamma_p {M_{p2}}^2\right) - \left(1+\gamma_p {M_{p1}}^2\right)}{\frac{1-\left(A_{p1}/A_{m3}\right)}{A_{p1}/A_{m3}}\left[\left(1+\gamma_s {M_{s1}}^2\right) - \frac{P_{s2}/P_{s0}}{P_{s1}/P_{s0}}^{\frac{1+\gamma_s}{A_{s1}/A_{s*}}}\right]} \quad (3.40)$$

3.4. Constant- Pressure Mixing Model

The principles that formed the basis of constant-pressure mixing approach were introduced by Keenan and Neumann [19]. One of the assumptions is that both primary and secondary streams are mixing with a uniform and constant pressure within the chamber. As shown in Fig. 9, the mixing chamber is between section 1 and section 2 within which the pressure is taken as being uniform. If the velocity of the fully mixed flow is supersonic ($M_{m2} > 1$), a normal shock wave is assumed to occur in the constant-area chamber between section 2 and section 3. The static pressure of the mixed flow leaving section 3 at uniform subsonic velocity is increased in the diffuser.

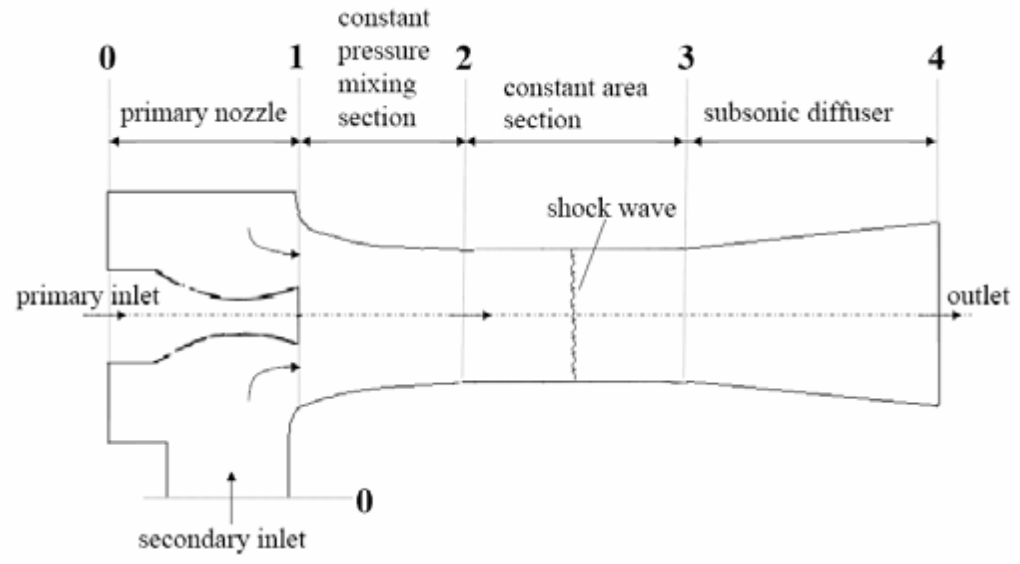

Fig. 9: Constant-pressure ejector flow model

Certain assumptions are necessary before deriving a model for the constant-pressure mixing ejector. These are:

(1) Conditions at the inlet for the primary and secondary streams, as well as the combined mixed output at the ejector's exit are both at stagnation.

(2) There is a uniformity in the velocities across all sections.

(3) Both streams mix at a constant pressure between sections 1 and 2.

(4) A shockwave will occur between sections 2 and 3 if there is a disparity between the flows at section 2 and 3. For instance, a supersonic mixed flow occurs at section 2 with a subsonic flow at section 3.

The equations for supersonic primary nozzle and subsonic diffuser in the constant pressure mixing ejector flow model are the same as those equations in the constant-area ejector model. This section will therefore focus on the equation derivations for the mixing process of the primary stream and secondary stream. Fig. 10 shows how the equations conserving continuity, energy, and momentum, are consolidated along with the perfect gas relations under the aforementioned assumptions and applied to analyze the control volume's flow field.

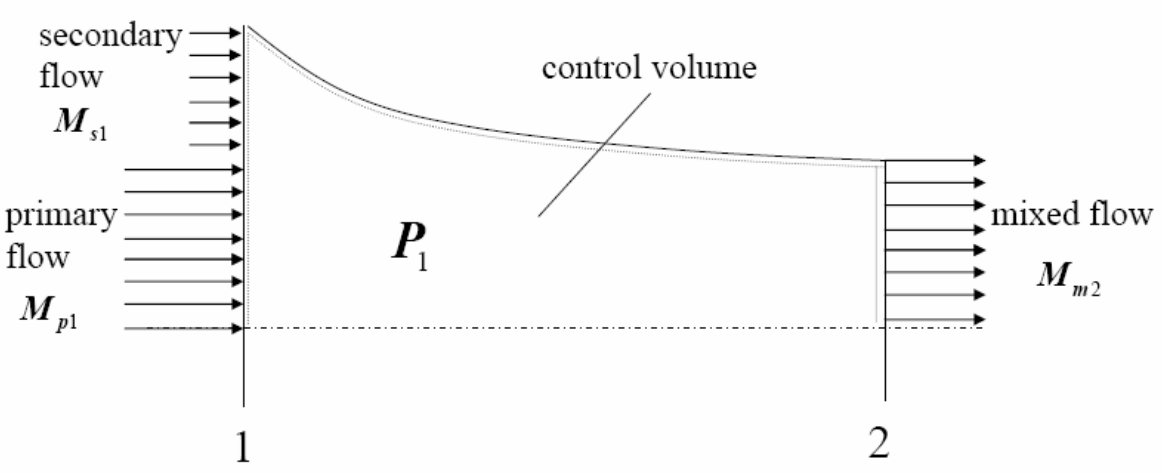

Fig. 10: Control volume of constant-pressure mixing chamber

According to the constant-pressure assumption,

$$P_{p1} = P_{s1} = P_{m1} = P_1 \tag{3.41}$$

Therefore, the mass flow ratio of secondary to primary at the inlet of the mixing chamber Equation (3.10) can be simplified to:

$$\omega = \frac{A_{s1}}{A_{p1}} \left(\frac{T_{p0}}{T_{s0}}\right)^{\frac{1}{2}} \left(\frac{R_p}{R_s}\right)^{\frac{1}{2}} \frac{f_2(\gamma_s, M_{s1})}{f_2(\gamma_p, M_{p1})} \tag{3.42}$$

Where, $f_2(\gamma, M)$ is the mass flow function defined by Equation (3.11); M_{p1} and M_{s1} are given by the following equations:

$$M_{p1} = \sqrt{\frac{2}{\gamma_p - 1} \frac{\eta_n \left[1 - \left(\frac{P_1}{P_{p0}}\right)^{\frac{\gamma_p - 1}{\gamma_p}}\right]}{1 - \eta_n \left[1 - \left(\frac{P_1}{P_{p0}}\right)^{\frac{\gamma_p - 1}{\gamma_p}}\right]}} \tag{3.43}$$

$$M_{s1} = \sqrt{\frac{2}{\gamma_s - 1}\left[\left(\frac{P_1}{P_{s0}}\right)^{-\frac{\gamma_s - 1}{\gamma_s}} - 1\right]} \tag{3.44}$$

The area ratio of the secondary stream to the primary stream can be obtained by rearranging Equation (3.42).

$$\frac{A_{s1}}{A_{p1}} = \left(\frac{T_{s0}}{T_{p0}}\right)^{\frac{1}{2}} \left(\frac{R_s}{R_p}\right)^{\frac{1}{2}} \frac{f_2(\gamma_p, M_{p1})}{f_2(\gamma_s, M_{s1})}\,\omega \tag{3.45}$$

The continuity equation for the selected control volume in Fig. 10,

$$m_{s1} + m_{p1} = m_{m2} \tag{3.46}$$

The area ratio of mixing chamber exit to the primary nozzle exit can be derived by substituting the mass flow function $f_2(\gamma, M)$ into Equation (3.46).

$$\frac{A_{m2}}{A_{p1}} = \left(\frac{T_{m0}}{T_{p0}}\right)^{\frac{1}{2}} \left(\frac{R_m}{R_p}\right)^{\frac{1}{2}} \frac{f_2(\gamma_p, M_{p1})}{f_2(\gamma_m, M_{m2})}\,(1 + \omega) \tag{3.47}$$

Where, R_m , γ_m and T_{m0} can be calculated by using Equation (3.16), Equation (3.17) and Equation (3.19), respectively. To design a constant-pressure gas ejector, it is desired to relate the entrainment ratio to the area ratio of the mixing chamber throat to the primary nozzle throat. This relationship can be derived by substituting Equation (3.9) and Equation (3.2) into Equation (3.48).

$$\frac{A_{m2}}{A_t} = \frac{A_{m2}}{A_{p1}} \frac{A_{p1}}{A_t} \tag{3.48}$$

$$\frac{A_{m2}}{A_{p1}} = \left(\frac{T_{m0}}{T_{p0}}\right)^{\frac{1}{2}} \left(\frac{R_m}{R_p}\right)^{\frac{1}{2}} \frac{(\gamma_p)^{\frac{1}{2}}}{f_2(\gamma_m, M_{m2})} \left(\frac{2}{\gamma + 1}\right)^{\frac{\gamma_p + 1}{2(\gamma_p - 1)}} \left[1 - \frac{(\gamma_p - 1)M_{p1}^2}{2\eta_n + \eta_n(\gamma_p - 1)M_{p1}^2}\right]^{\frac{-\gamma_p}{\gamma_p - 1}} (1 + \omega) \tag{3.49}$$

Since the static pressure in the mixing chamber is uniform and constant, the momentum conservation equation over the control volume in Fig. 10 can be simplified to be

$$m_{p1}V_{p1} + m_{s1}V_{s1} = m_{m2}V_{m2} \tag{3.50}$$

Considering the continuity equation as well as the definition of ω, Equation (3.48) can be further simplified to be

$$V_{p1} + \omega V_{s1} = (1+\omega)V_{m2} \tag{3.51}$$

The uniform velocity of the flow at the mixing chamber exit is

$$V_{m2} = \frac{V_{p1}+\omega V_{s1}}{(1+\omega)} \tag{3.52}$$

Using Mach numbers to substitute for the velocities in Equation (3.50),

$$M_{m2} = \frac{(M_{p1}+\omega M_{s1})\left(\frac{\gamma_s}{\gamma_p}\right)^{\frac{1}{2}}\left(\frac{R_s}{R_p}\right)^{\frac{1}{2}}\left(\frac{T_{s1}}{T_{p1}}\right)^{\frac{1}{2}}}{(1+\omega)\left(\frac{\gamma_m}{\gamma_p}\right)^{\frac{1}{2}}\left(\frac{R_m}{R_p}\right)^{\frac{1}{2}}\left(\frac{T_{m2}}{T_{p1}}\right)^{\frac{1}{2}}} \tag{3.53}$$

The $\frac{T_{s1}}{T_{p1}}$ and $\frac{T_{m2}}{T_{p1}}$ in above equation can be obtained by using the isentropic relationship between temperature and pressure:

$$\frac{T_{s1}}{T_{p1}} = \frac{T_{s0}}{T_{p0}}\left(\frac{P_{p0}}{P_1}\right)^{\frac{\gamma_p-1}{\gamma_p}}\left(\frac{P_{s0}}{P_1}\right)^{-\frac{\gamma_s-1}{\gamma_s}} \tag{3.54}$$

$$\frac{T_{m2}}{T_{p1}} = \frac{T_{m0}}{T_{p0}}\left(\frac{P_{p0}}{P_1}\right)^{\frac{\gamma_p-1}{\gamma_p}}\left(\frac{P_{m0}}{P_1}\right)^{-\frac{\gamma_m-1}{\gamma_m}} \tag{3.55}$$

The $\frac{T_{m0}}{T_{p0}}$ in Equation (3.53) can be calculated by using Equation (3.19). The $\frac{P_{m0}}{P_1}$ can be obtained by using the isentropic function:

$$\frac{P_{m0}}{P_1} = \left(1 + \frac{\gamma_m - 1}{2} {M_{m2}}^2\right)^{\frac{\gamma_m}{\gamma_m - 1}} \tag{3.56}$$

Substituting Equation (3.53) and Equation (3.54) into Equation (3.51), the Mach number at the mixing chamber exit is obtained:

$$M_{m2} = \frac{\xi}{\psi} \sqrt{1 - \frac{\gamma_m - 1}{2} \left(\frac{\xi}{\psi}\right)^2} \tag{3.57}$$

Where,

$$\xi = (M_{p1} + \omega M_{s1}) \left(\frac{\gamma_s}{\gamma_p}\right)^{\frac{1}{2}} \left(\frac{R_s}{R_p}\right)^{\frac{1}{2}} \left(\frac{T_{s1}}{T_{p1}}\right)^{\frac{1}{2}} \tag{3.58}$$

$$\psi = (1 + \omega) \left(\frac{\gamma_m}{\gamma_p}\right)^{\frac{1}{2}} \left(\frac{R_m}{R_p}\right)^{\frac{1}{2}} \left(\frac{T_{m0}}{T_{p0}}\right)^{\frac{1}{2}} \left(\frac{P_{p0}}{P_1}\right)^{\frac{\gamma_p - 1}{2\gamma_p}} \tag{3.59}$$

As previously mentioned, a shockwave can arise if there is a difference in velocity after constant-pressure mixing. For instance, a supersonic velocity with Mach number, i.e., $M_{m2} > 1$, will cause the formation of a normal shock wave sections 2 and 3. If this mixed flow then experiences an isentropic process, it will have a uniform pressure, denoted by $P_{m3,}$ in the constant-area section. Using gas dynamic relationships, we can derive follow parameters after the shockwave.

$$\frac{P_{m3}}{P_{m2}} = \frac{2\gamma_m}{\gamma_m + 1} {M_{m2}}^2 - \frac{\gamma_m - 1}{\gamma_m + 1} \tag{3.60}$$

$$\frac{T_{m3}}{T_{m2}} = \left(\frac{\gamma_m - 1}{\gamma_m + 1}\right)^2 \left(\frac{2\gamma_m}{\gamma_m - 1} {M_{m2}}^2 - 1\right) \left(\frac{2}{(\gamma_m - 1){M_{m2}}^2} + 1\right) \tag{3.61}$$

$${M_{m3}}^2 = \frac{{M_{m2}}^2 + \frac{2}{\gamma_m + 1}}{\frac{2\gamma_m}{\gamma_m - 1} {M_{m2}}^2 - 1} \tag{3.62}$$

3.5. Subsonic Diffuser

Nozzle efficiency, defined in Equation (3.2), has a similar definition to diffuser efficiency. This fact can be leveraged in order to obtain a ratio for the diffuser pressure:

$$\frac{P_{40}}{P_{m3}} = \left(1 + \eta_d \frac{\gamma_m - 1}{2} {M_{m3}}^2\right)^{\frac{\gamma_m}{\gamma_m - 1}} \tag{3.63}$$

Also, the combined compression ratio through the gas ejector can be calculated from the expression stated below:

$$\frac{P_{40}}{P_{s0}} = \frac{P_{40}}{P_{m3}} \frac{P_{m3}}{P_{p1}} \frac{P_{p1}}{P_{p0}} \frac{P_{p0}}{P_{s0}} \tag{3.64}$$

3.6. 1-Dimensional Models to Develop Ejector Design

Gas ejectors are incorporated into systems within highly specialized operational conditions and constraints. These are further dictated by specific temperature, pressure, and flow rate conditions. Any designed ejector must rigorously adhere to these restrictions and specifications in design.

The methodology of designing a gas ejector is extensive. The first step is to define the operating and boundary conditions. Next, we need to identify our desired ER and CR. The operational conditions directly factor into geometry of the the primary nozzle. From here, the focus shifts onto the mixing model, where we need to choose between the constant-area or constant-pressure approach. Once this is determined, we design the mixing chamber, keeping in mind the relationship between the ER and the AR. Lastly, the CR is used to delimit the dimensions of the diffuser.

Given the equations and quantities for constant-area/constant-pressure, either can be used to easily implement a design procedure.

A computer program, ESDUpac A9242 Version 2, developed and released by the Engineering Science Data Unit (ESDU) can be used to do the calculations for the ejector

design. All 1-D analytical models as well as their latest improvements are included in the package of ESDUpac A9242. Coefficient sets accrued across multiple experiments can be used as a correctional tool for various loss factors within calculations. It is a convenient and practical tool for gas ejector design and performance analysis.

ESDUpac A9242 provides the following design and performance prediction procedures.

Quick Design Procedure. Given a representative sample of quantities for entry and required exit pressures, temperatures, mass flow rates and dimensions the program will automatically solve for dimensions of the primary nozzle and exit using empirical data for air-air ejectors. The scope of Quick Design Method is restricted to ejectors with constant-area mixing and air as both working fluids.

Detailed Design Procedure. Give a representative sample for entry and required exit pressures, temperatures, mass flow rates, dimensions and loss factors as well as user defined constraints on the flow conditions, the software solves for dimensions at the primary nozzle and exit and flow conditions across the ejector.

Performance Prediction Calculation. Given the ejector dimensions, loss factors and a range of flow conditions at entry, the program will calculate the outlet conditions and the flow conditions through the ejector.

Fig. 11 is the typical gas ejector configuration utilized by ESDUpac A9242 for the calculations of design and performance prediction.

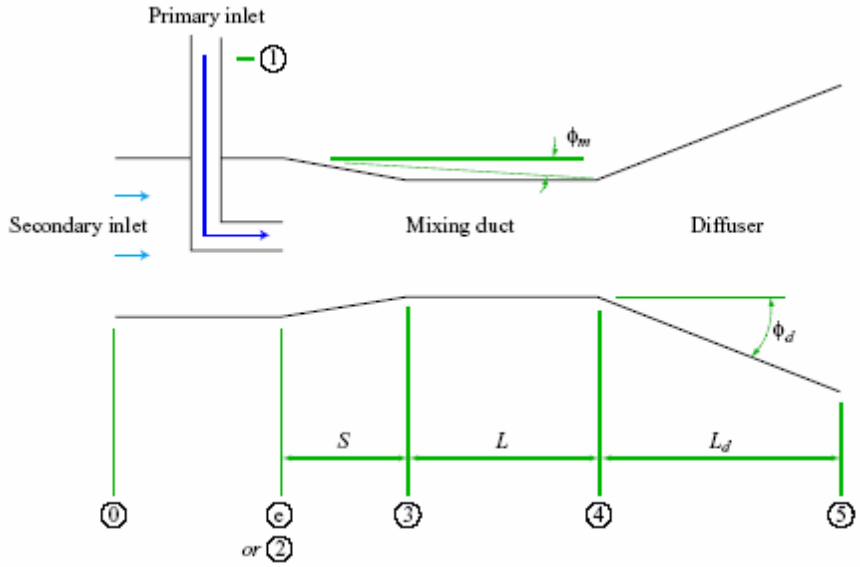

Fig. 11: Typical ejector configuration used by ESDUpac A9242

3.7. Summary

We have derived two different 1-D gas models in the above chapter, namely the constant-area mixing model and the constant-pressure mixing model using the conservation of mass, energy and momentum equations. The steps involved in this design were discussed above and the ESDUpac A9242 computer program was also introduced.

There is a popular belief that the constant-pressure mixing model results in designs with better performance. But the work presently done does not support this theory. Calculations presented above show that in certain working conditions the constant-pressure mixing model could have better performance while in others the reverse could be true. Also, Keenan and Neumann had an opinion that theoretical results based on the calculations of the constant-area flow model was in line and much more in agreement with the experimental results as compared to the constant-pressure model. In fact it was much more difficult to find this agreement in the theoretical and experimental results of the constant-pressure model.

In perfect conditions the perfect design method would provide information regarding the flow channel shape that would give the best results. However the reality is quite different, finding the optimal shape and dimensions of constant pressure mixing chamber are impossible. It might be possible to single out an operating condition and determine the geometry but that would work for only that condition. Changing a condition would require a complete re-design. Practically designing an ejector with the constant pressure approach is not feasible. Even though there were proposed modifications for that model there is still a need for improvement.

Designing and predicting the performance of an ejector, which is part of a system which has its own range of working conditions, requires more methods which are definitive. 2-D analytical methods could, theoretically be utilized, but they were ruled out due to the number of empirical coefficients required.

One method that is has become widely popular and is now much more easily available is Computational Fluid Dynamics (CFD). This method allows the modeling of complicated ejector geometries and the analysis gives better results, in turn allowing researchers to model complicated flows and gain a better understanding of the mixing process inside the ejector including local flow fields present.

4. Turbulence Models

4.1. Introduction

Turbulence, though already an established scientific recurring concept, is perhaps one of the most intriguing area in fluid dynamics. Contrarily, turbulence also has a profound disruptive influence in accurately simulating engineering flows, making it the toughest externality to regulate. Despite the advent of modern computing and extensive processing power at our disposal, the issue continues to evade us owing to its extreme complexity. Richard Feynman, Nobel-prize winning physicist, described turbulence as the "most important unresolved problem in classical physics."

Turbulence presents a problem because it is unfeasible to directly encompass the random nature and scale of the fluid's motion. The sheer computational power required makes any study significantly expensive and acts as a deterrent. For this reason, turbulence models become more important. Typically, CFD users are not concerned with a time-dependent solution of the system which can capture every vortex. These fluctuations act as noise affecting a holistic understanding of the system, which is why a steady-state solution is generally preferred as it looks at the system independent of time. Only through modeling can we resolve turbulent motions which are impacting the flow.

The type of models an individual use, can have a profound effect on the results of the simulations.

This happens because no model is perfect for every set of available conditions one encounters; each comes with its own set of constraints. Due to this, models continuously evolve and branch out into multiple iterations, each capturing a subset of the overall fluctuation in the system.

4.2. Families of Turbulence Models

Broadly speaking, turbulence models are classified into two categories, based on which governing equation they adhere to. This can either be the Reynolds-averaged Navier Stokes equations, or the Large Eddy Simulation equations. Further delimitation occurs on the basis of the additional transport equations, solutions of which are required to compute model contributions.

4.2.1. RANS-based turbulence models

4.2.1.1. Linear eddy viscosity models

4.2.1.1.1. Algebraic (Zero-Equation) Models

Algebraic models are the most straightforward and least taxing from a computational standpoint. They're often referred to as zero-equation models, since they do not require the addition of any transport equations to factor in turbulence contributions. In today's world, the usage of these types of models is very scarce however; upon application they do give excellent results

However, there is a catch to using these models. Because their components are derived directly from the flow variables, they miss out any influences on turbulence – such as convection and diffusion of turbulent energy – over a span of time. This makes such models unfeasible for use in general situations since they do not capture a complete picture. However, they are extremely useful if deployed for non-complex flow geometries or during the beginning computational phases as a means to set up broad parameter constraints for further tweaking through more specific models. Among the spectrum, the most popular equation models falling within this category are

- Baldwin Lomax model
- Cebeci - Smith Model.

Simpler models, written as $\mu_t = f(y^+)$, are employed in more particular cases like boundary layers or jets.

Another particular equation which is considered to fall within this category is the Johnson-King model. The equation utilizes the resolution of an ordinary differential equation, which is why some experts refer to it as a 1/2 equation model.

4.2.1.1.2. One-Equation Models

One-equation models, as the name suggests, involve solving a transport equation in order to obtain the turbulent viscosity. This added level of complexity increases the accuracy of the model, but also brings the concerns of computational power required to fully test the model. The original model within this category is the Prandtl one-equation model, but several iterations have arisen since. These include:

- Baldwin-Barth
- Spalart-Allmaras
- Rahman-Agarwal- Siikonen

The Spalart-Allmaras model is the most widely employed in this category, and also delivers better output in comparison to other models. The model derives its reliability by calculating each field point's distance to the nearest wall, which also improves the stability of the results. Alternatively, users can choose between the Baldwin-Barth and the Goldberg point-wise model for their needs.

While the Goldberg model skips calculating wall and field point distances, making it slightly faster in delivering results compared to Spalart-Allmaras, this comes at a cost. As mentioned, the Spalart-Allmaras model is more stable, making its results more trustworthy. However, this does not mean that the Goldberg model is useless.

One equation turbulence models typically target the same parameter of turbulent kinetic energy. Prandtl's one-equation model is the original one-equation model.

4.2.1.1.3. Two-Equation Models

Building upon the complexity from the previous section, two-equation models include two central equations which must be solved in order to evaluate the impact of turbulence upon the average flow. Apart from the Spalart-Allmaras model, this category constitutes the vast majority of models used to simulate turbulence. Commonly found models are the Menter SST model and the k-epsilon model, and a plethora of other models, for varying other engineering applications, are also found in use.

The SST model amalgamates the k-omega and k-epsilon model, which are used to model interactions occurring in regions near to and far from walls respectively. Because of this added layer of calculation, the solution produces robust results on a consistent basis. Among all models present, the SST model is also the best at capturing recirculation regions.

The k-epsilon model, the most wide spread of them all, is aptly called a conglomeration of models. Dedicated types have been developed for usage in places so galore that the specific flow configurations employ almost as many different k-epsilon models, as there are CFD practitioners trying to implement them in solving ranging problems. Some of the clichéd add-ons including the Jones-Launder, Chien, and RNG k-epsilon models are in practice.

The Reynolds number is used as a measure of a model's ability to be used within boundary layers and beyond. Models not possessing a "low Reynolds number" classification typically entail the addition of extra functions specifically for the walls in order to correctly and completely account for the effect of viscous walls.

Two equation turbulence models are among the most widespread models currently available. In fact, the k-epsilon and k-omega models are considered a benchmark within the industry and are employed for a broad variety of engineering problems. However, work continues on identifying ways to enhance the accuracy of these equations at marginal cost to computing power, making this a hotspot for current research.

In order to fully represent the flow's turbulent properties, two-equation models compute two additional transport equations. This is useful as it makes the model time dependent, allowing the analysis to include parameters like turbulent energy convection and diffusion.

As mentioned earlier, one of the most commonly sought parameters is the turbulent kinetic energy, which is represented by k. Choices for the next transported variables include turbulent or specific dissipation – epsilon or omega respectively. Both variables work in tandem to determine the amount of energy within the turbulence and the scale of the turbulence as well. Here scale refers to its demarcation between length and time.

4.2.1.1.3.1. K-epsilon Model

The K-epsilon model is one of the most common turbulence models, though it is unable to deliver high quality results in scenarios involving adverse pressure gradients. This two equation model makes use of the turbulent kinetic energy and epsilon, representing the turbulent dissipation, within its additional transport equations to fully evaluate the scale and energy within the turbulence.

The "Standard K-epsilon Model" was conceived by Launder and Sharma and comprises one major interpretation of the model. It was intended as an improvement to the mixing-length model, with the added focus of identifying alternatives which could relate turbulent length scales in moderate to high complexity flows in algebraic terms.

While the K-epsilon model has its advantages, its utility is fairly limited when considering problems in inlets and compressors. This is because the model demonstrably produces the finest results when pressure gradients within free-shear flows are small. Similarly the accuracy of the results show a declining trend for wall-bounded and internal flows in situations where the pressure gradients are increased or if the system contains adverse pressure gradients. The concluding inference is that the K-epsilon model is not a suitable choice for inlets and compressors, as they can experience shockwaves due to disparate pressures which are mostly beyond the model's threshold for computation.

To calculate boundary conditions for these models see turbulence free-stream boundary conditions.

For turbulent kinetic energy k

$$\frac{\partial}{\partial t}(\rho k) + \frac{\partial}{\partial x_i}(\rho k u_i) = \frac{\partial}{\partial x_j}\left[\left(\mu + \frac{\mu_t}{\sigma_k}\right)\frac{\partial k}{\partial x_j}\right] + P_k + P_b - \rho\epsilon - Y_M + S_k$$

For dissipation ϵ

$$\frac{\partial}{\partial t}(\rho\epsilon)+\frac{\partial}{\partial x_i}(\rho\epsilon u_i)=\frac{\partial}{\partial x_j}\left[\left(\mu+\frac{\mu_t}{\sigma_\epsilon}\right)\frac{\partial\epsilon}{\partial x_j}\right]+C_{1\epsilon}\frac{\epsilon}{k}\left(P_k+C_{3\epsilon}P_b\right)-C_{2\epsilon}\rho\frac{\epsilon^2}{k}+S_\epsilon$$

4.2.1.1.3.2. K-omega Model

The more widely applied two-equation model in turbulence flow is the K-omega model. It is similar to the K-Epsilon model insofar as requiring the computation of two additional central equations to account for a fluid's turbulent flow's properties. But it varies from the K-Epsilon model in the choice of the second variable.

Turbulent kinetic energy, denoted by 'k', is the obvious first parameter being accounted for in a transport equation. Unlike the K-Epsilon model, however, this model focuses on a quantity called the specific dissipation, ω, as its second variable. The entry of the second variable allows the model to focus on specific interactions closer to the walls, thereby defining the scale of the system within which turbulence is being observed. The turbulent kinetic energy determines, for the system, the overall amount of energy in it.

4.2.1.2. Nonlinear eddy viscosity models

For the RANS equations This is a class of turbulence models, which utilize additional coefficients to signify values of eddy viscosity. These are used to bridge mean turbulence fields to mean velocity fields in a non-linear fashion, mathematically represented by:

$$-\rho\left\langle u_i u_j\right\rangle = 2\,\mu_t\,\mathcal{F}_{nl}\left(S_{ij},\Omega_{ij},\dots\right)$$

Where

- $\mathcal{F}_{nl}$ is a nonlinear function possibly dependent on the mean strain and vorticity fields or even other turbulence variable
- μ_t is the coefficient termed turbulence "viscosity" (also called the eddy viscosity)

- $S_{ij} = \frac{1}{2}\left[\frac{\partial U_i}{\partial x_j} + \frac{\partial U_j}{\partial x_i}\right] - \frac{1}{3}\frac{\partial U_k}{\partial x_k}\delta_{ij}$ is the mean strain rate
- $\Omega_{ij} = \frac{1}{2}\left[\frac{\partial U_i}{\partial x_j} - \frac{\partial U_j}{\partial x_i}\right]$ is the mean vorticity

4.2.1.3. Reynolds stress model (RSM)

The Reynold's Stress Models (RSM) are considered the most comprehensive and complex turbulence models. They are also known as the Reynold's Stress Transport (RST) models, The approach for this type of modeling was initiated by Launder's work in 1975. They employ a unique method of closure typically referred to as a Second Order Closure. Within this model, eddy viscosity values are discarded all stress fields are calculated directly, making this a more computationally taxing approach. However, given that transport equations representing the Reynolds stress are quite precise and calculated directly, the directional effects of Reynolds stress fields also become accessible within the results. This adds a deeper layer of analysis but comes at the expense of computational cost.

The Reynolds involves differential transport equations which must be categorically solved in order to understand the individual Reynolds stresses, represented by $\overline{\rho u_i' u_j'}$. These findings are then engaged to determine the closure within a momentum equation which has been Reynolds-averaged.

4.2.1.3.1. Scale-Resolving Simulation

While a large majority of CFD simulations are based on Reynolds Averaged Numerical Solution models, there are some subsets or classes of flows which are more elaborately explained by models which set aside a specific portion of the numerical domain within which they place the turbulence spectrum. Methods like these are known as scale-resolving simulation models or SRS models.

The general argument which is portrayed is that RANS models are very strong in the analysis of flows which are bounded by walls. In these particular cases, the calibration of the experiment within the laws of the wall form a solid basis upon which further sifting and refining can be done to extract meaningful data.

However, free-shear flows do not align themselves as neatly, creating a highly non-uniform situation. Among the plethora of examples are the plain self-similar flows like jets. Mixing layers and wakes which impinge flows are also harder to model with RANS equation systems. If you bring in flows which possess a strong swirl quality, or flows which are massively separated, the situation begins to stretch further outside the capability of the typical RANS model. While one could employ the RSM model in each of these cases, it will be to little effect given that the reliability of the data will drop too significantly to hold any value.

In the case of free-shear flows, it is considerably less difficult to solve for the largest turbulent scales, since these are roughly of the same order as a shear layer's thickness. Contrastingly, this length scale diminishes in relation to the boundary layer's thickness as one approaches closer to the wall, a phenomenon which is observed in more pronounced effect if we increase the Re number as well. LES models are extremely limited as a result of this condition, since we do not currently possess the computational power required to provide a tangible and actionable output. In order to simplify the process and make it easier to tackle, a lot of active research is being carried out in the field of hybrid models. These incorporate elements from both LES and RANS models, applying them to the relevant portions of the system, namely away from the wall and at boundary layers respectively.

4.2.2. Large eddy simulation (LES)

4.2.2.1. Introduction

Large eddy simulation (LES) are among the most widely accepted and applied simulation models for demonstrating turbulent flows. They follow as an extension of Kolmogorov's (1941) theory of self-similarity, which implies that large eddies of the flow are highly dependent on the inherent geometry of the system, whereas the smaller scales are more

common and widespread. Exploiting this assumption, LES models utilize a sub grid-scale (SGS) model to tacitly factor in all impacts of small eddies, while more explicitly solving the system for large eddies.

In mathematical terms, this translates into a distinction of the velocity field in to resolved and sub-grid components. The first component – namely the resolved component – deals primarily with the large eddies; the second – sub-grid – component tackles the question of eddies occurring on a smaller scale. In more explicit mathematical terms, this can be represented as the convolution of a function which contains a filtering kernel G:

$$\bar{u}_i(\vec{x}) = \int G(\vec{x} - \vec{\xi}) u(\vec{\xi}) d\vec{\xi},$$

resulting in

$$u_i = \bar{u}_i + u_i',$$

Where $\bar{u}_i$ represents the resolvable scale component and u_i' becomes the sub grid-scale component. In most practical or commercial scenarios however, the LES model is not implemented in exactly this form. In fact, the standard seems to have become to use the grid itself as a filter without any other explicit attempts at doing so.

The filtered equations are derived directly from the incompressible version of the Navier-Stokes equations of motion:

$$\frac{\partial u_i}{\partial t} + u_j \frac{\partial u_i}{\partial x_j} = -\frac{1}{\rho}\frac{\partial p}{\partial x_i} + \frac{\partial}{\partial x_j}\left(\nu \frac{\partial u_i}{\partial x_j}\right).$$

Substituting in the decomposition $u_i = \bar{u}_i + u_i'$ and $p = \bar{p} + p'$ and then filtering the resulting equation gives the equations of motion for the resolved field:

$$\frac{\partial \bar{u}_i}{\partial t} + \bar{u}_j \frac{\partial \bar{u}_i}{\partial x_j} = -\frac{1}{\rho}\frac{\partial \bar{p}}{\partial x_i} + \frac{\partial}{\partial x_j}\left(\nu \frac{\partial \bar{u}_i}{\partial x_j}\right) + \frac{1}{\rho}\frac{\partial \tau_{ij}}{\partial x_j}.$$

While a critical assumption in this situation is of the commutative properties of the filtering and differentiating operations, we observe that this is not the general case since there are

implicit errors which also trickle in. These discrepancies are miniscule, and have been further reduced due by the discovery of new filters which commute with differentiation. The additional partial derivative term $\partial \tau_{ij} / \partial x_j$ is derived from the non-linear advection terms, due to the fact that

$$\overline{u_j \frac{\partial u_i}{\partial x_j}} \neq \bar{u}_j \frac{\partial \bar{u}_i}{\partial x_j}$$

and hence

$$\tau_{ij} = \bar{u}_i \bar{u}_j - \overline{u_i u_j}$$

Similar equations can be derived for the sub-grid-scale field (i.e. the residual field).

Sub grid-scale turbulence models usually employ the Boussinesq hypothesis, and seek to calculate (the deviatory part of) the SGS stress using:

$$\tau_{ij} - \frac{1}{3}\tau_{kk}\delta_{ij} = -2\mu_t \bar{S}_{ij}$$

where $\bar{S}_{ij}$ is the rate-of-strain tensor for the resolved scale defined by

$$\bar{S}_{ij} = \frac{1}{2}\left(\frac{\partial \bar{u}_i}{\partial x_j} + \frac{\partial \bar{u}_j}{\partial x_i}\right)$$

and ν_t is the sub-grid-scale turbulent viscosity. Substituting into the filtered Navier-Stokes equations, we then have

$$\frac{\partial \bar{u}_i}{\partial t} + \bar{u}_j \frac{\partial \bar{u}_i}{\partial x_j} = -\frac{1}{\rho}\frac{\partial \bar{p}}{\partial x_i} + \frac{\partial}{\partial x_j}\left([\nu + \nu_t]\frac{\partial \bar{u}_i}{\partial x_j}\right),$$

where we have used the incompressibility constraint to simplify the equation and the pressure is now modified to include the trace term $\tau_{kk}\delta_{ij}/3$.

4.2.2.2 Sub-grid-scale models

Some examples are:

Smagorinsky model (Smagorinsky, 1963)

Algebraic dynamics model (Germano, et al., 1991)

Dynamic Global power factor model (You and Moin , 2007)

Localized dynamic model (Kim and Menon, 1993)

WALE (Wall-Adapting Local Eddy-viscosity) model (Nicoud and DUCROS, 1999)

RNG- LES model

Structural Modeling

4.2.3. Detached eddy simulation (DES)

We've already discussed the limitations inherent in the LES models when trying to simulate turbulent flows in near-wall regions. We've also mentioned how hybrid models are being developed in order to bypass these technicalities. Such models hinge upon a combination of the best aspects of Reynolds Average Numerical Solutions and Large Eddy Solution models to iron out all minor discrepancies and present a better, stable data picture as its output. The Detached-Eddy simulation is one such instance of a hybrid approach [Spalart et al (1997)]. By combining the RANS and LES equation systems, the model is able to optimize the way it treats near-wall regions and the remainder of the flow. The model was originally formulated by replacing the distance function d in the Spalart-Allmaras (S-A) model with a modified distance function

$$\tilde{d} = \min[d, C_{\mathrm{DES}}\Delta],$$

Where CDES is a constant and Δ is the largest dimension of the grid cell in question. With this basic tweak into the Spalart-Allmaras model we are allowed access to a significantly new

way of interpreting the system. This is because the modified distance function enables the model to behave like an RANS model in regions close to walls, and in a Smagorinsky-like manner away from the walls. Such a duality in behavior is best explained with arguments which show that the model's scale dependence is localized rather than broadened or made "global". This is further substantiated through a dimensional analysis of the system.

If a model has a turbulence flow with a well-defined turbulence length scale, and is constrained to a reasonable degree, the DES method can be applied for a solution or simulation. This is different from the Spalart-Allmaras model in the way it treats the length scale of the turbulence and its characterization. The Baldwin-Barth model, which shares a host of similarities to the S-A model, is contrarily not a suitable choice to be used with DES. The reasoning is that the standard form of the model also encompasses van Driest-sort damping capacities which make separation work difficult. Menter's SST model can act as a decent hopeful.

The Menter SST model obtains a length scale of the turbulence from the model's mathematical outputs, combines it with the length scale of the entire framework, and contrasts it and the framework length scale to switch in the middle of LES and RANS. When translated into practical terms, this entails extensive programming and recalibration than merely according a change in the length scale's calculations. Another advantage of the DES method is that it specifically assigns regions to either RANS or LES category. This overrules the distance function. Also, many implementations use different differencing in RANS regions (e.g. up-winded differences) and LES regions (e.g. central differences).

4.2.4. Direct Numerical Simulation (DNS)

A Direct numerical simulation (DNS) is a reenactment in computational liquid flow in which the Navier-Stokes comparisons are numerically explained in the absence of a turbulence model. This implies that the entire scope of three-dimensional and worldly scales of the turbulence must be determined. All of the turbulence's spatial scales must be determined in the computational lattice, including the littlest dissipative scales (Kolmogorov scales), up to the essential scale L, connected by movements comprising the greater part of the motor vitality. The Kolmogorov scale, η, is given by

$$\eta = (\nu^3/\varepsilon)^{1/4}$$

in this equation, ν indicates the kinematic viscosity while ε connotes the rate at which kinetic energy dissipates. In comparison, the integral scale is contingent upon the boundary conditions and their spatial scale.

The number of points (N) along a given direction on the mesh with increments (h), must be

$$Nh > L,$$

to satisfy these resolution requirements, in order for the integral scale to be contained within the computational domain, and also

$$h \leq \eta,$$

In order for the Kolmogorov scale to be resolved.

Since

$$\varepsilon \approx u'^3/L,$$

where u' is the root mean square (RMS) of the velocity, the previous relations imply that a three-dimensional DNS requires a number of mesh points N^3 satisfying

$$N^3 \geq \mathrm{Re}^{9/4}$$

where Re is the turbulent Reynolds number

$$\mathrm{Re} = \frac{u'L}{\nu}.$$

One of the caveats of using this method is that it requires an immense amount of memory for storage of the output, especially when considering an increasing Reynolds number. Furthermore, the solution must be integrated using explicit methods to retain accuracy. To accomplish this, integration is typically carried out using a time step, Δt, which is small enough, so as to make a fluid particle move only a fraction of, h, the mesh spacing in each step. I.e.,

$$C = \frac{u'\Delta t}{h} < 1$$

The Courant Number is represented by C

The interval of total time simulated is proportional to,τ, the turbulence time scale written as

$$\tau = \frac{L}{u'}.$$

Merging these equations, along with the fact that h must be of the order η, the required number of time-integration steps must be generally proportional to $L/(C\eta)$. On the other hand, from the given definitions of Re, η and L shown above, we can see that

$$\frac{L}{\eta} \sim \mathrm{Re}^{3/4},$$

Consequently, the number of time steps grows along as well, as a power law of the Reynolds number.

One can estimate that the number of floating-point operations required to complete the simulation is proportional to the number of mesh points and the number of time steps, and in conclusion, the number of operations grows as Re^3.

4.3. Turbulence near-wall modeling

4.3.1. Wall Functions

An important component of wall function simulations is the y plus value for a given cell. Standard simulations require that the first cell beyond the walls possess a y plus value in the log-layer, beginning at y plus 20 and extending to approximately y plus 200 depending on the Re number. The log layer represents a balancing point between the competing forces of the kinetic energy's production and dissipation, and acts as a contributing factor in stabilizing the turbulence in near-wall simulations.

4.3.2. Low-Re resolved boundary layers

Running a simulation which has a low-Re number typically requires that boundary layers are fully resolved and all boundary layer meshes are completely refined. Another condition which must be adhered to is that the y plus value of the first cell at the walls must be less than 1, and that all cells outside the walls must be kept at values below 1.25 even if they are being stretched.

4.3.3. Turbulence free-stream boundary conditions

In most CFD recreations it is important to indicate estimations of the turbulence variables at the deltas. For instance, on the off chance that you are utilizing a model you need to indicate estimations of and at the gulfs. This is regularly troublesome and a wellspring of instability since the approaching turbulence is once in a while known precisely. Regularly you are compelled to make a pretty much taught theory of the approaching turbulence. Assessing the turbulence model variables, in the same way as turbulent vitality, dissemination or Reynolds stresses, specifically is frequently troublesome. Rather it is simpler to think as far as variables like the approaching turbulence force and turbulent length scale or vortex thickness proportion. These properties are more natural to comprehend and can all the more effectively be identified with physical attributes of the issue.

4.4. Summary

Turbulence modeling continues to be one of the most active forces pushing the boundaries of Computational Fluid Dynamics. Industrial CFD code applications are increasingly demanding models which can provide a balanced approach, which can not only enclose physical effects of turbulence but do so within the constraints of limited computational power availability and an efficient turnaround time for the end users at an industrial level. For the majority of applications, RANS models continue to act as the go-to choice for the most optimal results which neatly juggle computational resources along with accuracy. Any further refinement will be carried out with the objective of expanding simulations to include phenomena such as anisotropy within turbulence while retaining the same calibration levels as present models.

Another hotspot for research will be developing systems that can accurately identify laminar-turbulent transitions. There is a dire need for models which can yield high accuracy results, and one possible way to deliver on this objective is to bring in CFD applications which test laminar-turbulent transition processes as well.

Perhaps the most ardent push in the area of Computational Fluid Dynamics will be that of scale-resolving simulation (SRS) models. Existing codes in the industry must begin to cater to a wider range of advanced formulations across a spectrum which goes from SAS and DES all the way to more complex zonal methods which also account for interface conditions. All of these will also have to actively seek opportunities to scale the models in accordance with an increase in Re number flows while retaining computational economy. Wall-modeled LES may continue to be a focal point of future research for this very reason.

5. CFD Methodology

5.1. Computational Methodology

For the numerical investigations, an axisymmetric domain from the axis to the wall of the two-stage ejector is considered. The model is created using the commercial CFD package Design-Modeler integrated into ANSYS Workbench 14.5, and the governing equations are solved using FLUENT, which employs the finite volume method to discretize the governing equations. The boundary conditions prescribed for the simulations are listed. A segregated implicit solver with a $k-\omega$ turbulence model has been employed to compute the flow pattern inside the two-stage ejector system. The only additional simplification invoked in the present study is that fluid properties are assumed as constant, since the rocket exhaust flow rate is much smaller than the air flow rates used for pumping in the ejectors. In other words, temperature variations are not very high ($T < 100$ K) for these flow conditions. Simulations have been carried out until the residues fall below 1×10^{-6} for all the flow variables. The simulations have been carried out during no-flow (initial startup of rocket motor) and full flow (steady state operation of rocket motor). The atmospheric pressure condition is imposed at the ejector exit. The basic fluid flow equations that govern the axisymmetric compressible flow in a second throat ejector-diffuser system are given below.

Continuity Equation

$$\frac{1}{r}\frac{\partial}{\partial r}(\rho r v_r) + \frac{\partial}{\partial z}(\rho v_z) = 0$$

r-Momentum Equation

$$\rho\left(v_r\frac{\partial v_r}{\partial r} + v_z\frac{\partial v_r}{\partial z}\right) = -\frac{\partial P}{\partial r} + \left(\frac{1}{r}\frac{\partial}{\partial r}(r\tau_{rr}) + \frac{\partial \tau_{rz}}{\partial z}\right) + \frac{\tau_{\theta\theta}}{r}$$

z-Momentum Equation

$$\rho\left(v_r\frac{\partial v_z}{\partial r} + v_z\frac{\partial v_z}{\partial z}\right) = -\frac{\partial P}{\partial z} + \left(\frac{1}{r}\frac{\partial}{\partial r}(r\tau_{rz}) + \frac{\partial \tau_{zz}}{\partial z}\right)$$

Energy Equation

$$\rho\left(v_r\frac{\partial}{\partial r}\left(e+\frac{P}{\rho}\right)+v_z\frac{\partial}{\partial z}\left(e+\frac{P}{\rho}\right)\right)=-\frac{1}{r}\frac{\partial}{\partial r}(rq_r)-\frac{\partial q_z}{\partial z}+\mu\phi$$

In the above equations,

$$\tau_{rr}=\mu\left(2\frac{\partial v_r}{\partial r}-\frac{2}{3}(\Delta.v)\right)$$

$$\tau_{rz}=\tau_{zr}=\mu\left(\frac{\partial v_z}{\partial r}+\frac{\partial v_r}{\partial z}\right)$$

$$\tau_{zz}=\mu\left(2\frac{\partial v_z}{\partial z}-\frac{2}{3}(\Delta.v)\right)$$

$$\tau_{\theta\theta}=\mu\left(2\frac{v_r}{r}-\frac{2}{3}(\Delta.v)\right)$$

$$q_r=-k\frac{\partial T}{\partial r}$$

$$q_z=-k\frac{\partial T}{\partial z}$$

$$\phi=2\left[\left(\frac{\partial v_r}{\partial r}\right)^2+\left(\frac{\partial v_z}{\partial z}\right)^2\right]+\left(\frac{\partial v_z}{\partial r}+\frac{\partial v_r}{\partial z}\right)^2$$

5.2. Modeling, Meshing and Analysis

5.2.1. Modeling

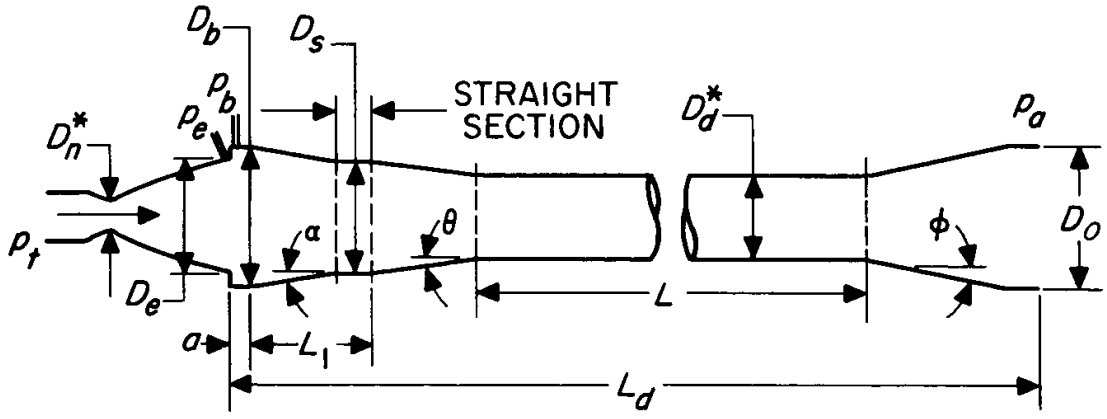

Fig. 12: Supersonic Exhaust Diffuser

$D_b/D_e = 1.126$ $\quad D_s/D_e = 1.005$ $\quad L_1/D_s = 1.00$

$\psi = 1.545$ $\quad L/D_d^* = 10.00$ $\quad D_o/D_d^* = 2.00$

$\alpha = 5$ deg $\quad \theta = 5$ deg $\quad \phi = 10$ deg

$a/D_e = 0.0704$ $\quad L_d/D_e = 13.1$

CONFIGURATION 3

This configuration for the STED was selected out of the four configurations put forward by Roschke et al. in his report in 1962 in which experimental work was performed to determine the most optimum configuration for exhaust diffusers for rocket engines.

5.2.1.1. System Model

We used ESDUpac A9242 to come up with the remaining system model, which was basically the model for the two stage ejector system, with the initial conditions mentioned in the figure. This figure below is a rough sketch of the system that was simulated.

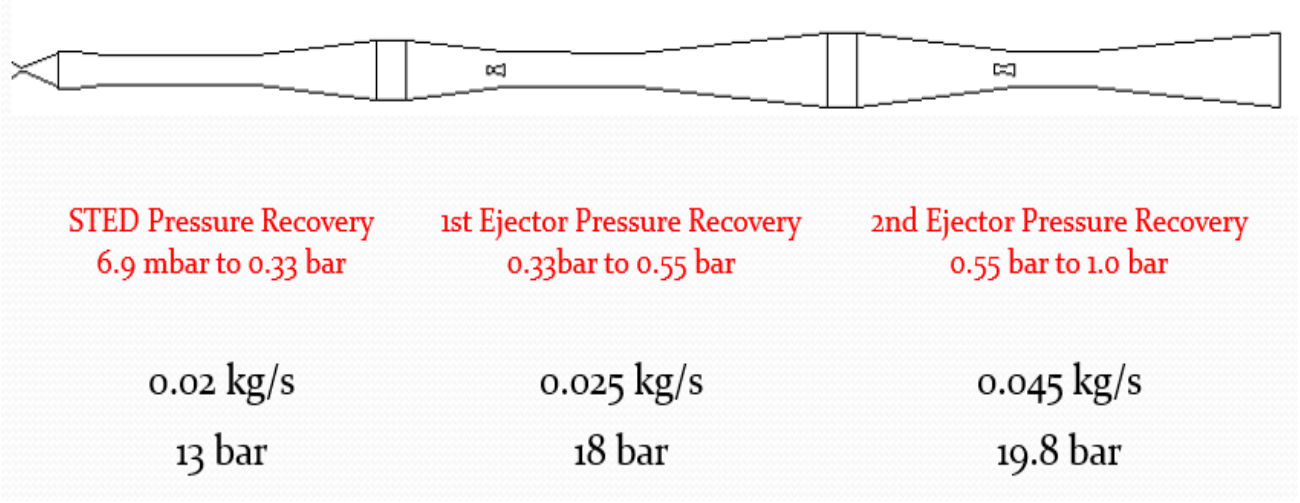

Fig. 13: Cold Gas Subscale System

We used Nitrogen as the main working fluid in all the three nozzles shown above in the figure. Its static temperature would be at 300K.

5.2.1.2. Design Parameters

Table 1: Design Parameters

Parameter	Measure
Main nozzle flow rate	0.02 kg/s
Main nozzle static pressure	13 bar
1st Ejector nozzle flow rate	0.025 kg/s
1st Ejector nozzle static pressure	18 bar
2nd Ejector nozzle flow rate	0.045 kg/s
2nd Ejector nozzle static pressure	19.8 bar
Exit static pressure	1 bar
Fluid (all nozzles)	Nitrogen
Fluid static temperature (all nozzles)	300 K

5.2.1.3. ESDUpac A9242 Design Solution

Table 2: Design Solution

Parameter	Measure
Main nozzle exit to throat area ratio	7.8055
1st Ejector nozzle exit to throat area ratio	2.7096
2nd Ejector nozzle exit to throat area ratio	2.3472
STED static pressure recovery	0.3231 bar
1st Ejector static pressure recovery	0.22 bar
2nd Ejector static pressure recovery	0.45 bar

5.2.2. Meshing

5.2.2.1. Mesh Generation

The Mesh was generated using ANSYS ICEM. A structured mesh was generated with clustering around the walls and nozzles.

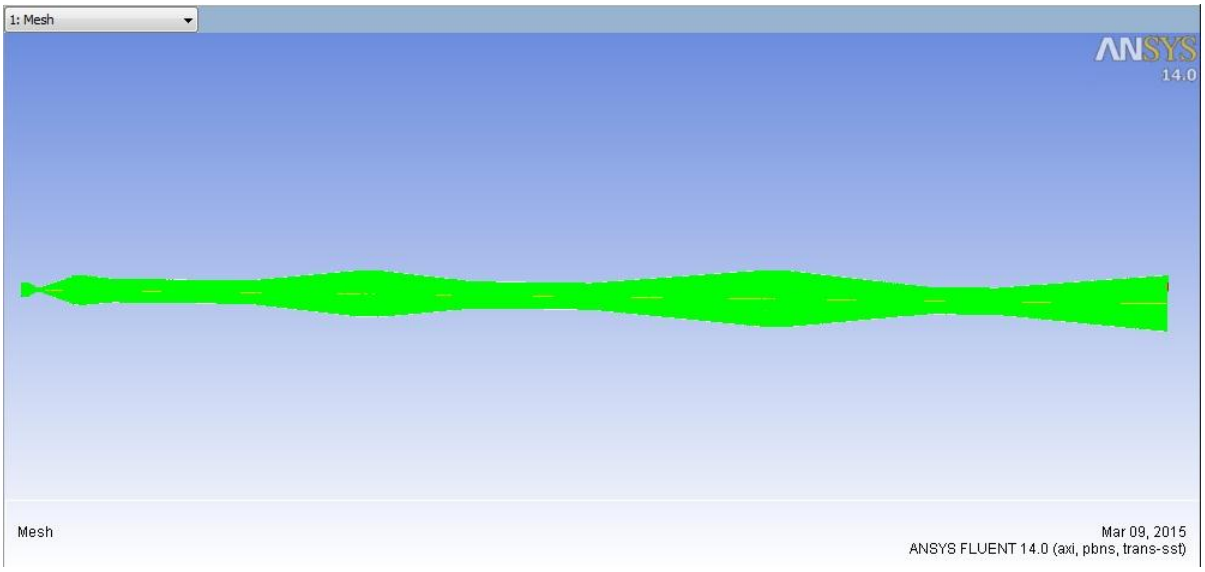

Fig. 14: HAT complete Mesh

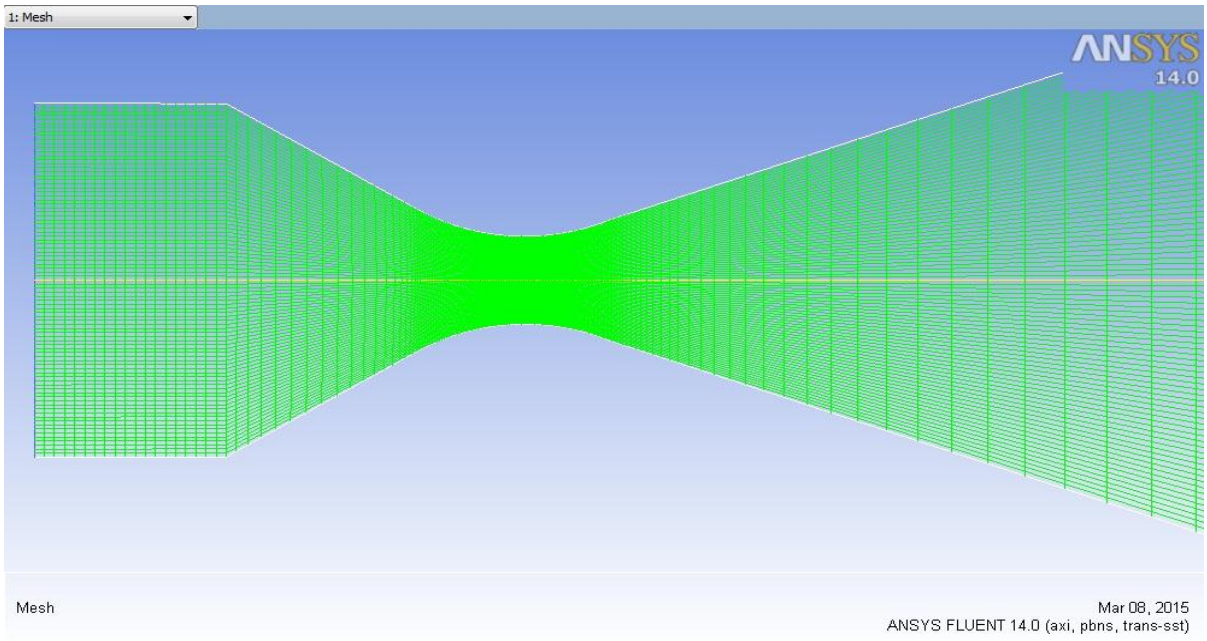

Fig. 15: Close up of Primary Nozzle Mesh

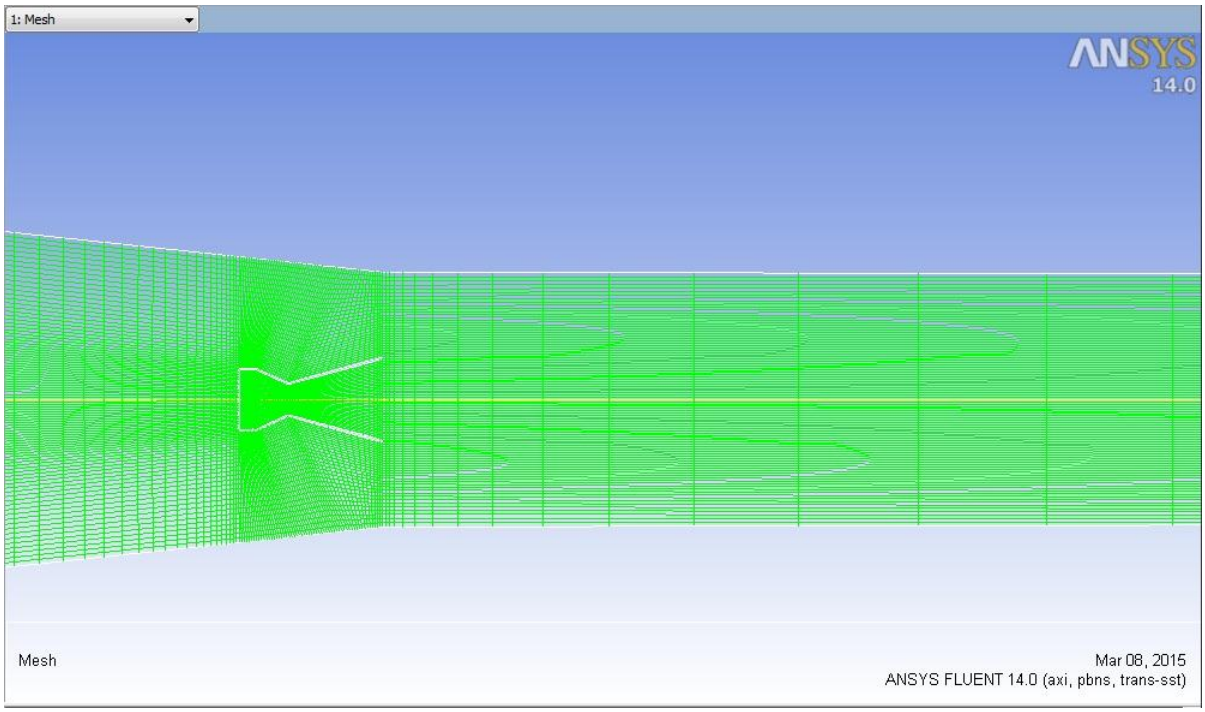

Fig. 16: Close up of First Ejector Nozzle Mesh

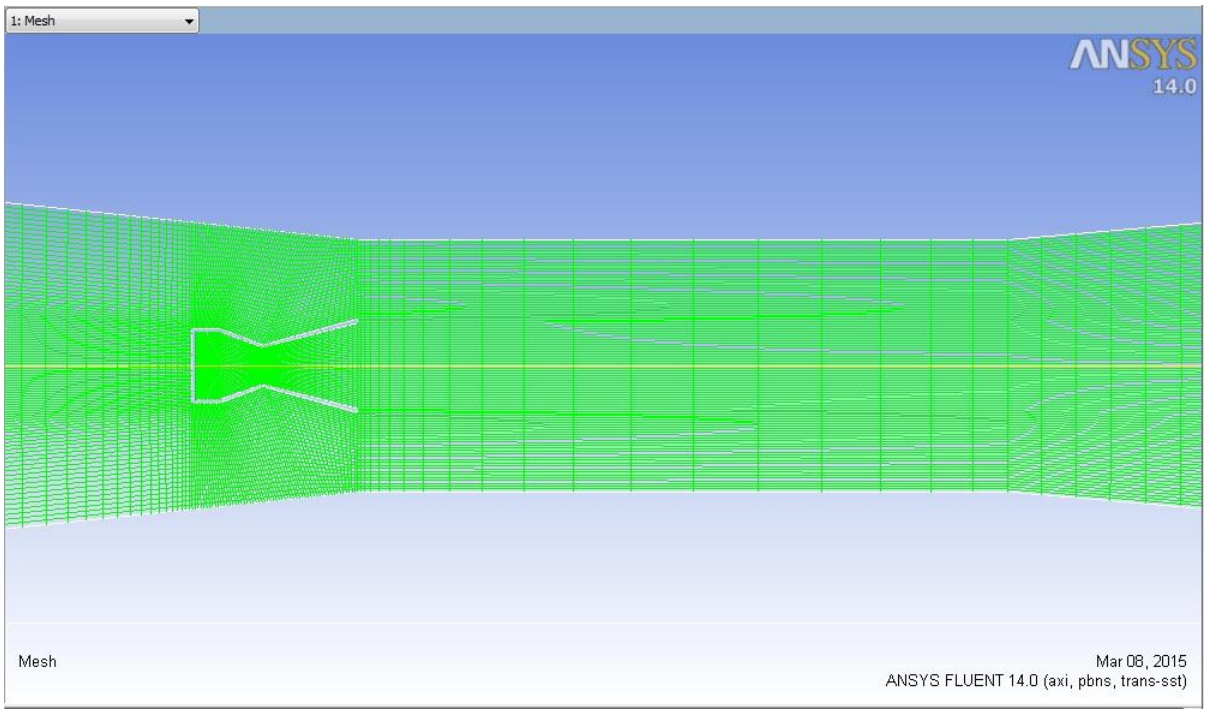

Fig. 17: Close up of Second Ejector Nozzle Mesh

5.2.2.2. Grid Adaption

The solution-adaptive mesh refinement feature of FLUENT allows you to refine and/or coarsen your grid based on geometric and numerical solution data. In addition, FLUENT provides tools for creating and viewing adaption fields customized to particular applications. The adaption process is described below. We specifically used the Gradient Based Grid Adaption process for our mesh.

5.2.2.2.1. Gradient Adaption

The primary goal of solution-adaptive grid refinement is to efficiently reduce the numerical error in the digital solution. Unfortunately, direct error estimation for point-insertion adaption schemes is difficult because of the complexity of accurately estimating and modeling the error in the adapted grids. Assuming the greatest error occurs in high-gradient regions, the readily available physical features of the evolving flow field may be used to drive the grid

adaption process. The equidistribution adaption technique used by FLUENT multiplies the undivided Laplacian of the selected solution variable by a characteristic length scale [256]. The length scale is the square (2D) or cube (3D) root of the cell volume. The introduction of this length scale permits resolution of both strong and weak disturbances, increasing the potential for more accurate solutions.

5.2.3. Viscous models

FLUENT offers five viscous models, these are as stated below:

1. Spalart-Allmaras model

2. k-ε models

- Standard k-ε model

- Renormalization-group (RNG) k-ε model

- Realizable k-ε model

3. k-ω models

- Standard k-ω model

- Shear-stress transport (SST) k-ω model

4. Reynolds stress model (RSM)

5. Large eddy simulation (LES) model

Riffat et al. used FLUENT to investigate how the positioning of the primary nozzle's exit affected the performance of an ejector. Riffat et al., during the CFD modeling chose to adopt the standard k-ε − model and Renormalization Group (RNG) k-ε − model to solve the turbulence problems at hand.

FLUENT was also used by Bartosiewicz et al. al in their simulations of ejectors, but in their conclusion the shear stress transport (SST) version of the k-ω − turbulence model agreed best with the test data of the ejector.

So for these simulations we made use of the (SST) version of the k-ω − turbulence model.

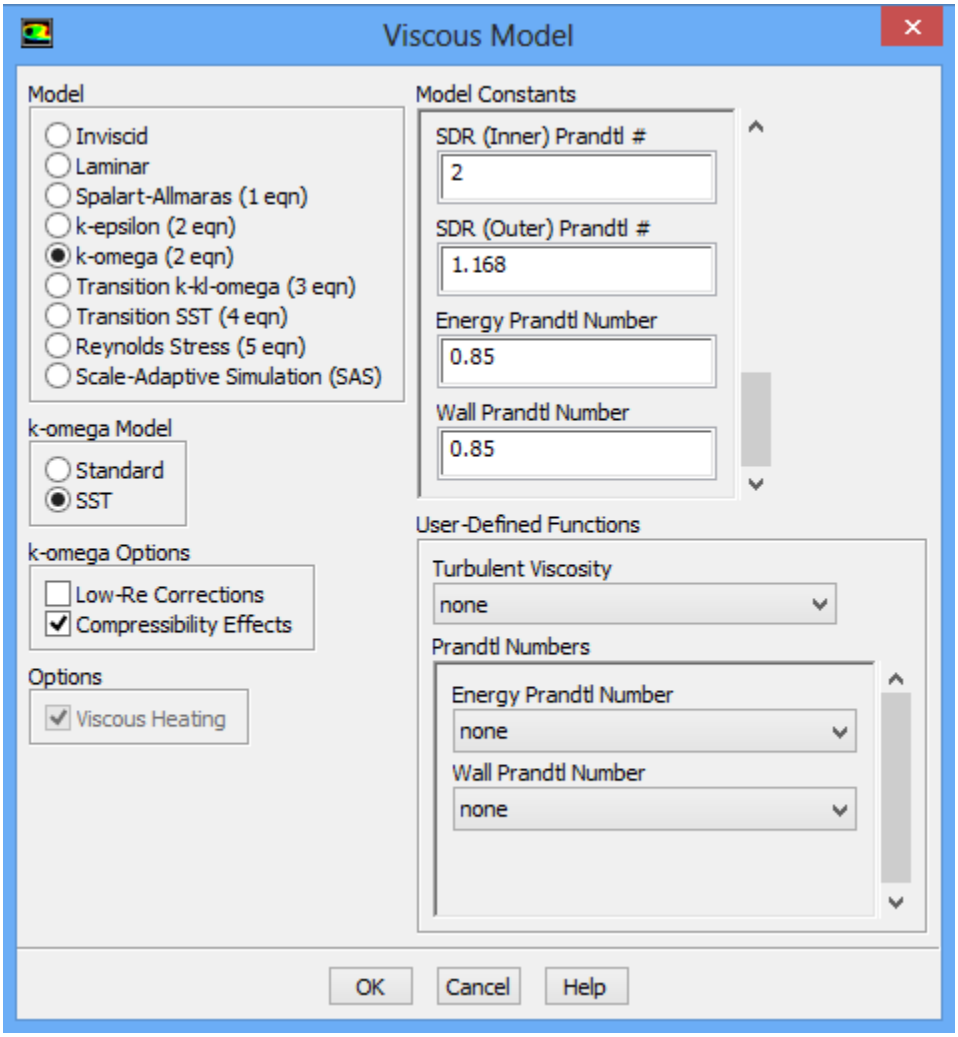

Fig. 18: Viscous model settings

5.2.4. Simulations

5.2.4.1. Method

All parameters were set at first order discretization initially. They were converted to second order discretization as soon as the solution converged.

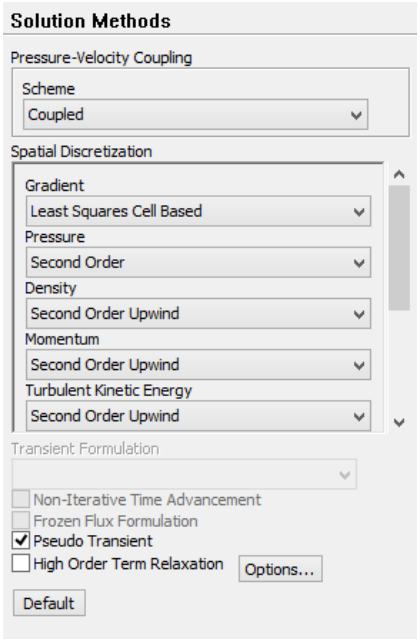

Fig. 19: Solution Method

5.2.4.2. Solution Controls

Table 3: Solution Controls

Pressure	0.05
Momentum	0.05
Density	0.1
Body Forces	0.1
Turbulent Kinetic Energy	0.075
Specific Dissipation Rate	0.075
Intermittency	0.075
Momentum Thickness Re	0.075
Turbulent Viscosity	0.1
Energy	0.075

5.2.4.3. Convergence monitors

Iterations were carried out until the residuals fell below 10-6 for all the variables being calculated.

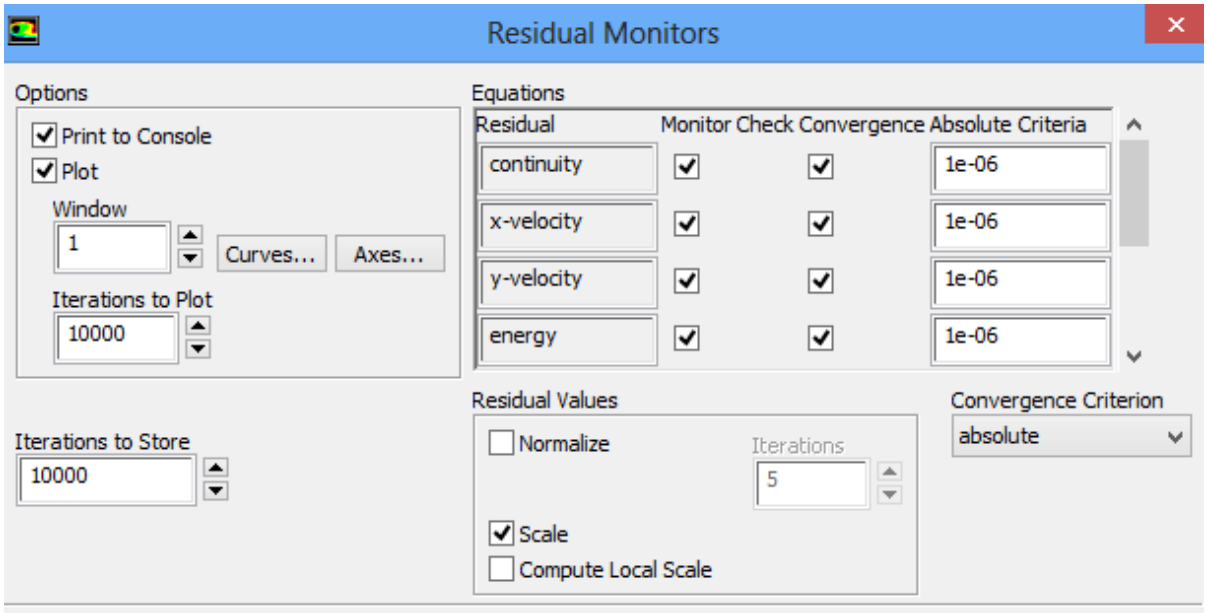

Fig. 20: Residual Monitors Settings

5.2.4.4. Simulation Steps

The simulations were run in the following manner:

1. With the main nozzle on and both ejectors off, the first simulation was simply a test run, with a back pressure of 1 bar, to check how the main nozzle operated and the flow behaved. The expected outcome was that flow separation would occur early on indicating the starting of the nozzle. To achieve this, the nozzles in both ejectors were set as walls instead of mass flow inlets.
2. After that, the main simulation was performed in a series of steps which are indicated as follows:
    a. Ejector E2 was turned on while E1 and the main nozzle were both off, we iterated until the solution became steady

b. Then E1 was turned on while E2 was still operating and we continued iterating till the solution became steady again
c. And finally with both the ejectors running we turned on the main nozzle and continued iterating. With this we observed the flow of the thruster and saw if flow separation occurred and how the thruster performed with two-stage ejection.

5.2.4.5. Flow chart for simulations

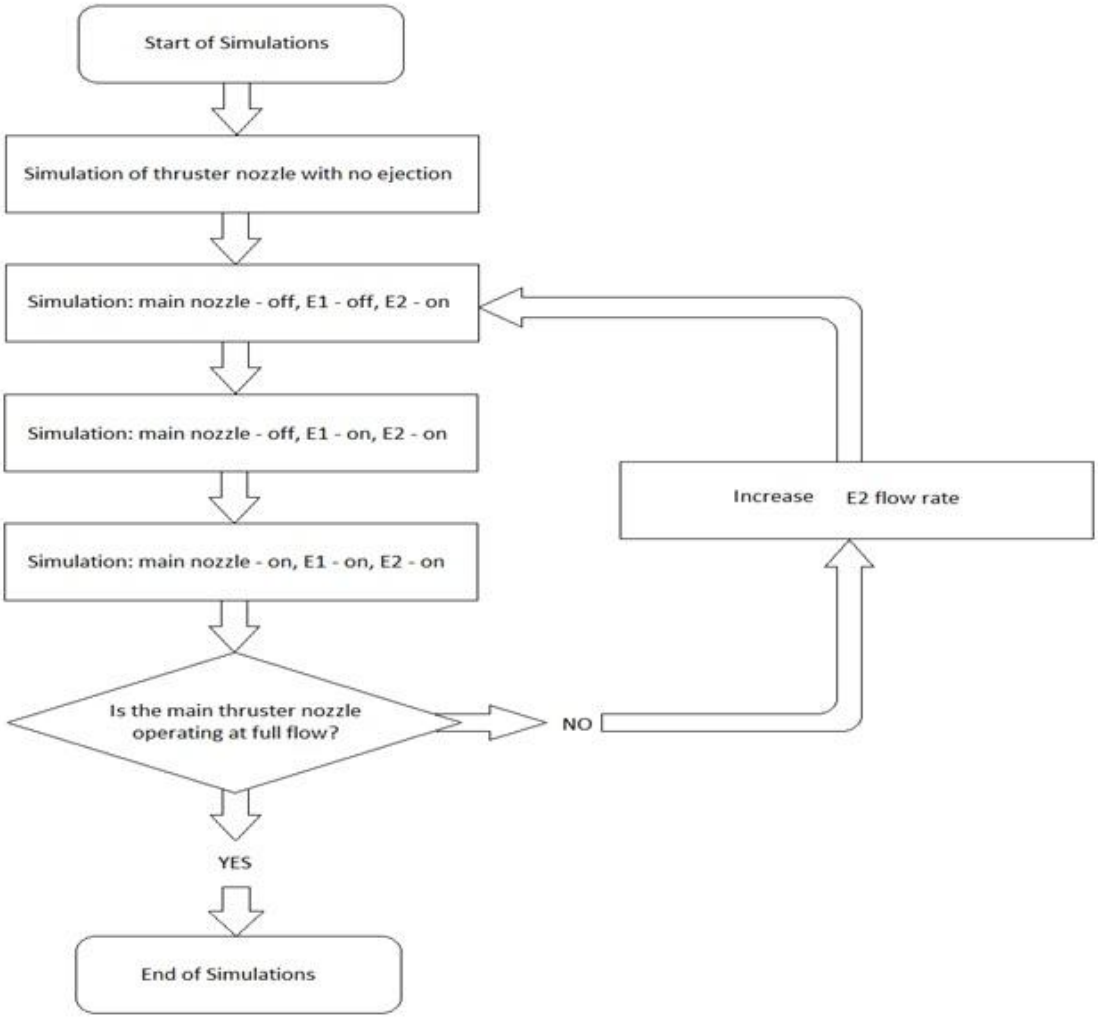

Fig. 21: Solution Flow Diagram

6. Analysis and results

6.1. Simulations

6.1.1. Trial No. 1

Before the main simulations were started, a sort of dry run was performed to confirm that flow separation would occur without the two-stage ejection. For this only the main nozzle was turned on and allowed to flow. Fig. 22 and fig. 23 confirm this.

After this initial run, we proceeded to the original steps of the solution process. Working with the original conditions provided, we ran the simulations according to the steps mentioned in 5.2.4.4.

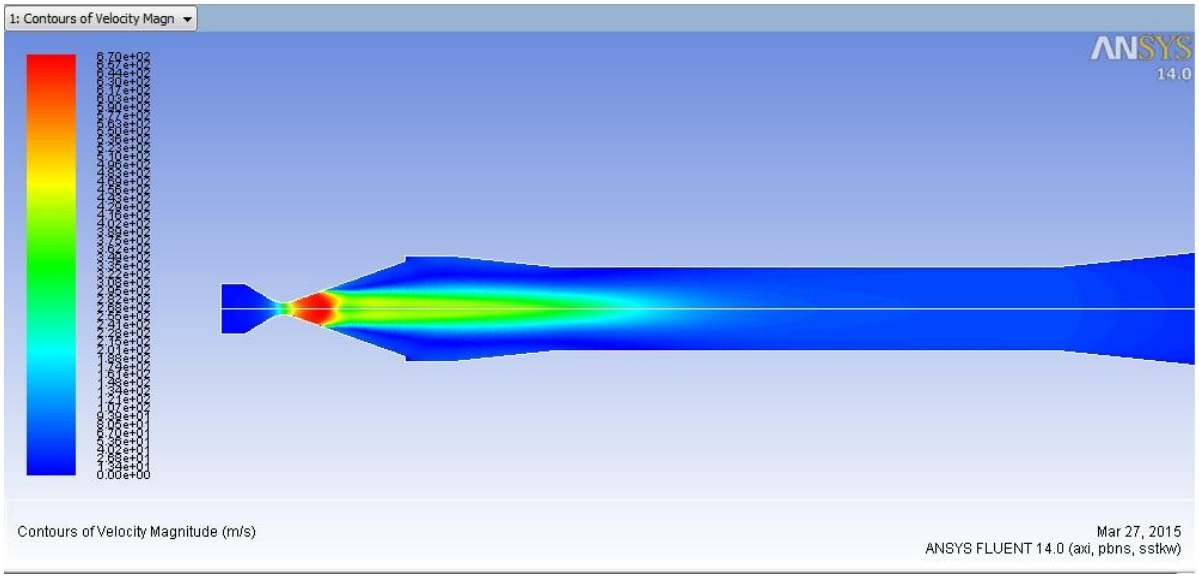

Fig. 22: Main Nozzle on Only-Velocity

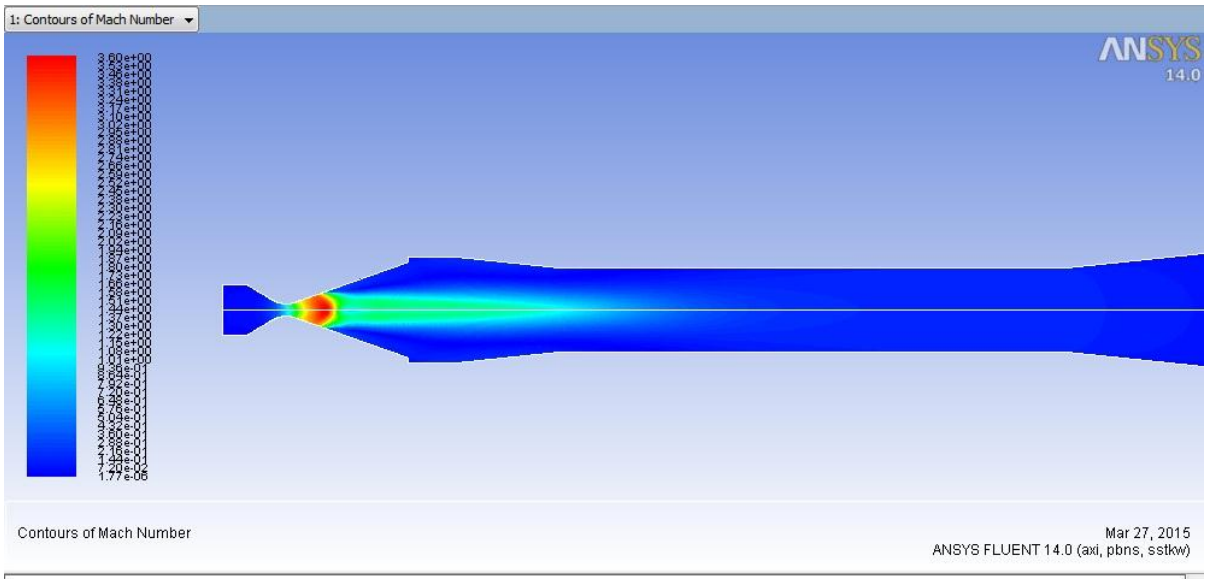

Fig. 23: Main Nozzle on Only-Mach Number

The STED was designed to provide a small amount of ejector action by slightly offsetting the inlet diameter from the main nozzle outlet diameter. This can be observed in fig. 22 and fig. 23. This allowed the exhaust of the main nozzle to be used to evacuate the chamber. But even with this offset the ejector action of the STED is not enough to fulfill the vacuum requirements of the test chamber. The required value of 3 mbar pressure was not even remotely achieved with the given conditions.

6.1.1.1. Simulation of the primary nozzle with two-stage ejection

This is done in the following 3 step process:

1. Simulation: Main nozzle – off, E1 – off, E2 – on
2. Simulation: Main nozzle – off, E1 – on, E2 – on
3. Simulation: Main nozzle – on, E1 – on, E2 – on

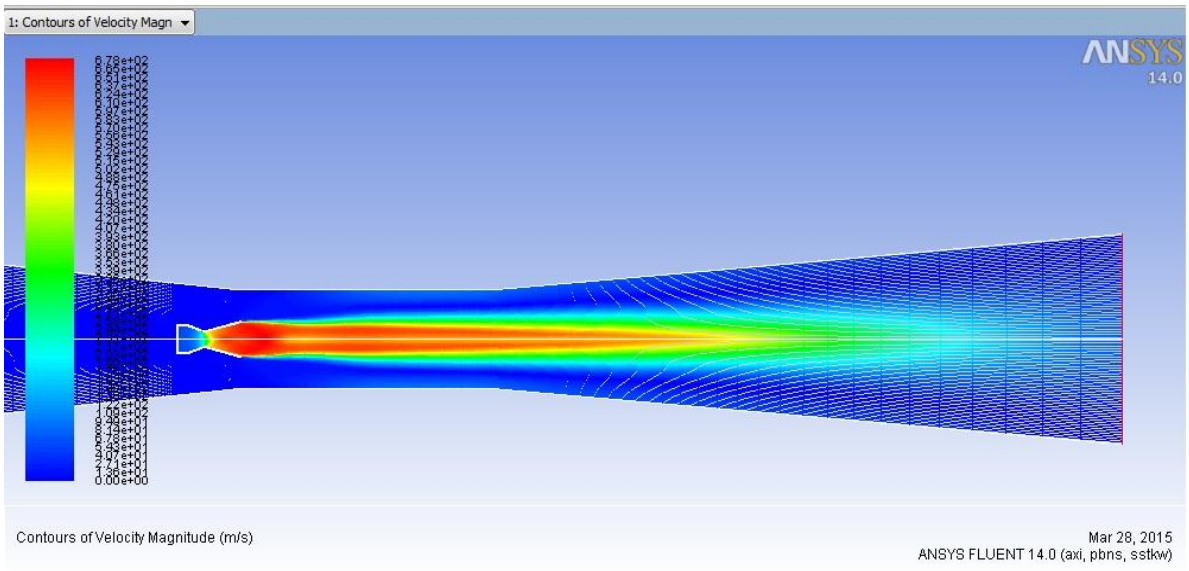

Fig. 24: E2 on Only-Velocity

From fig. 24 and 25 we see that, at the conditions provided the ejector has a flow that can be characterized as an ambient flow. There is no visible flow separation occurring in the flow of the second ejector. It shows that the second ejector has started up properly.

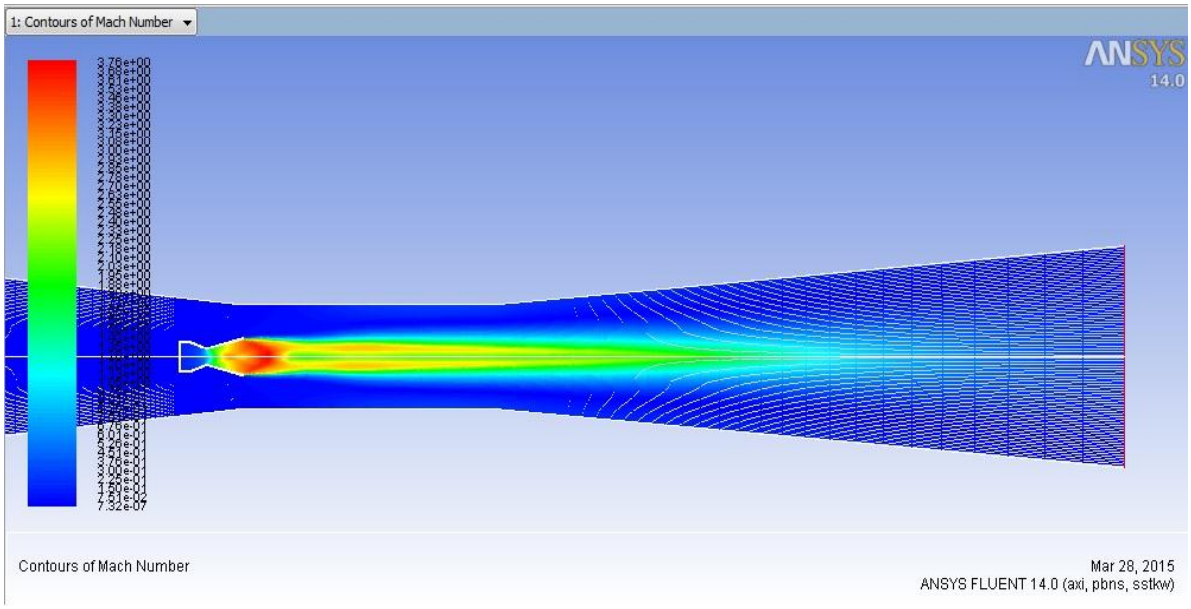

Fig. 25: E2 on Only-Mach Number

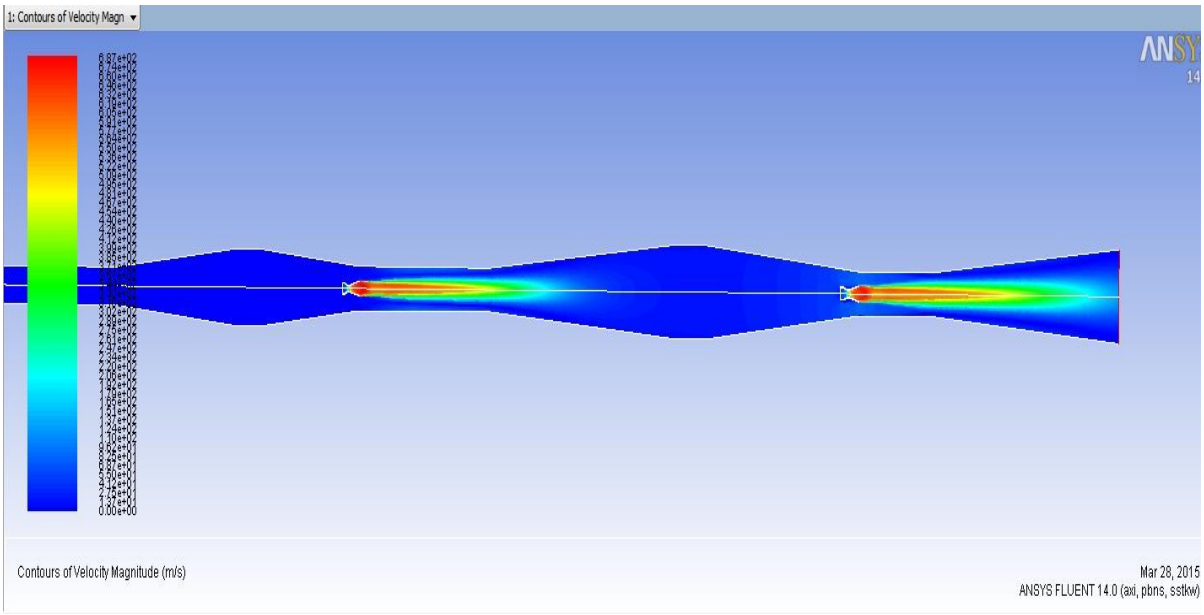

Fig. 26: E1 & E2 on-Velocity

Fig. 26 and 27 show that, after the start of the second ejector the first ejector is started as soon as full flow for the second ejector is achieved. With this step the two stage ejector system becomes fully operational. However using the provided boundary conditions we observe that even with the ejectors working properly the vacuum level achieved in the test chamber is still not adequate to get a proper start-up of the main thruster nozzle. The vacuum level achieved is about 20 mbars using the two stage ejection alone.

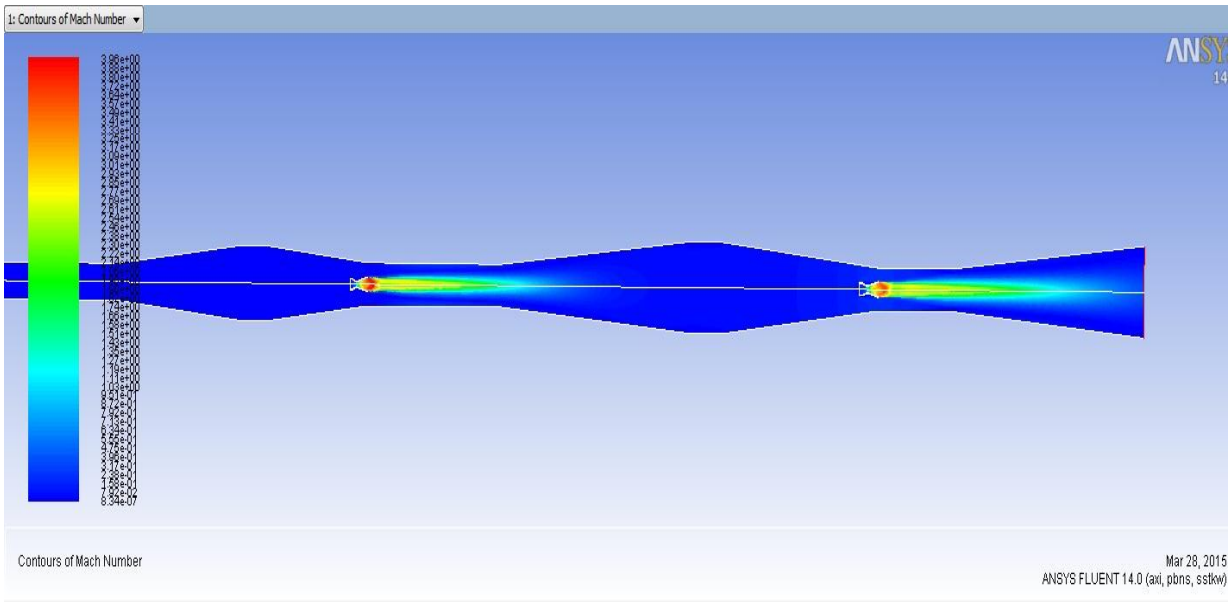

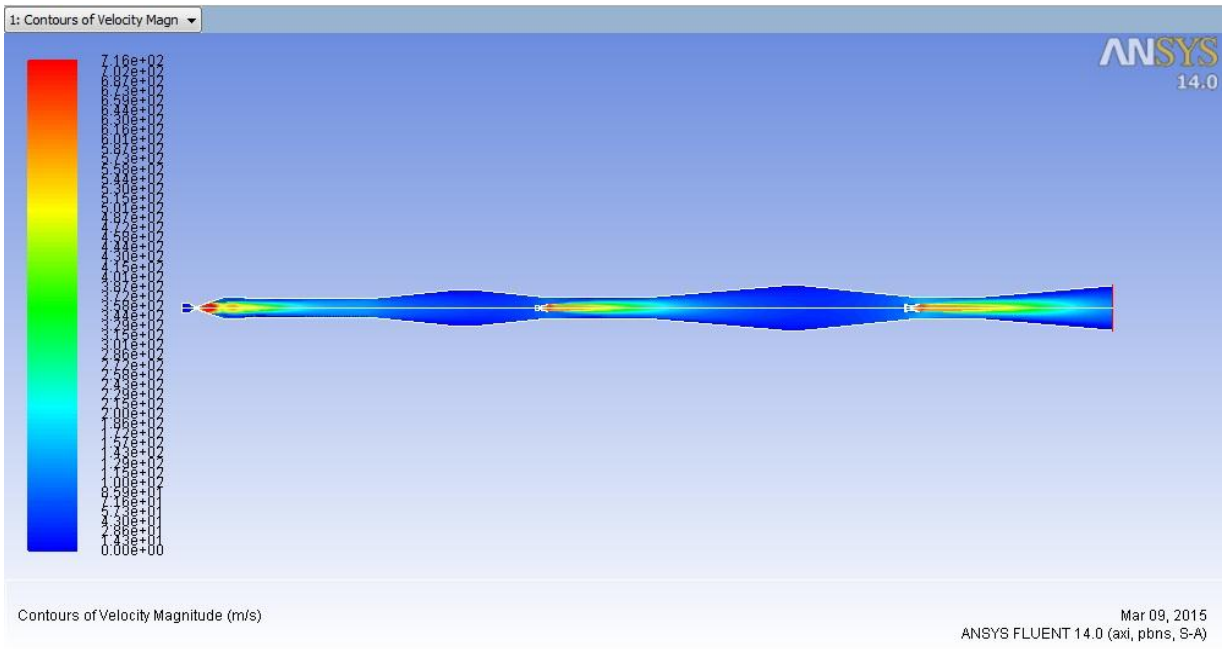

Fig. 28: All Nozzles on-Velocity

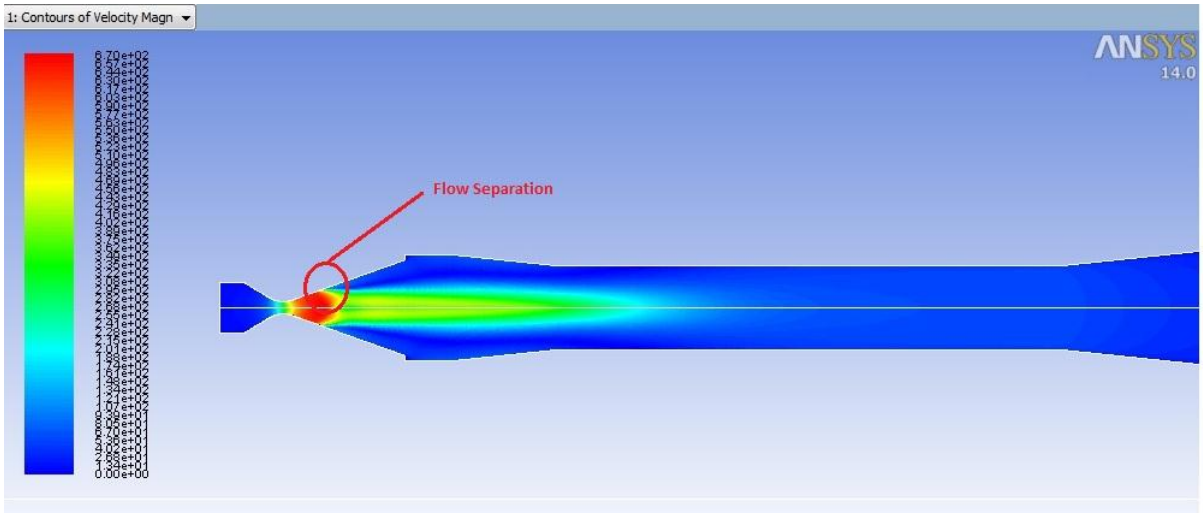

Fig. 29: Flow Separation in the Main Nozzle

6.1.1.2. Results of Trial No. 1

We followed the steps mentioned above and from fig. 28 we see that the performance improved significantly but from the figure we still observe flow separation and full flow is still not achieved.

6.1.2. Trial No. 2

From the results of Trial No. 1 we observe that full flow was not achieved at the conditions provided initially. So the flow rates were increased. We increased the rate of the main nozzle to 0.022 kg/s and the rate of the 2nd ejector to 0.047 kg/s to satisfy the ideal entrainment condition where the sum of the main nozzle and the 1st ejector nozzle mass flow rates equals the mass flow rate in 2nd ejector nozzle. Even though the goal of this thesis was to see if the main nozzle operates under the conditions provided, two additional trials were performed just to verify whether adjustment was required in the design conditions or the design of the facility itself.

Table 4: Boundary Conditions for Trial no. 2

Boundary	Boundary Condition	
	Type	Measure
Main nozzle inlet	Mass flow inlet	0.022 kg/s, 14.3 bar
1st Ejector inlet	Mass flow inlet	0.025 kg/s, 18 bar
2nd Ejector inlet	Mass flow inlet	0.047 kg/s, 19.8 bar
Exit	Pressure outlet	1 bar
Wall-zone	Wall	-
1st Ejector wall	Wall	-
2nd Ejector wall	Wall	-
Axis-line	Axis	-

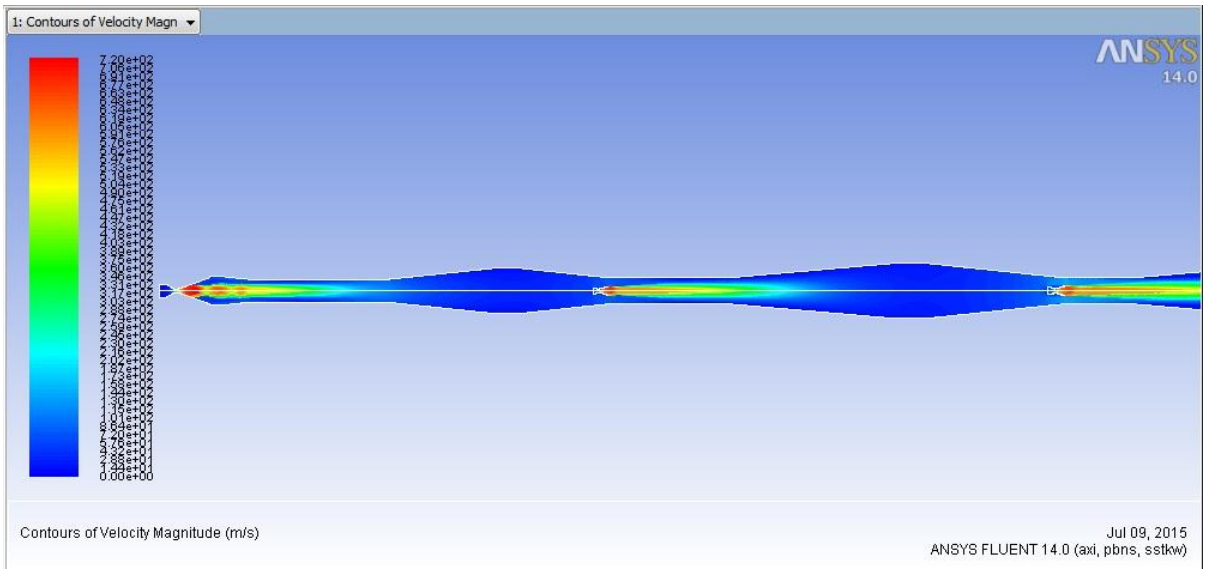

Fig. 30: All Nozzles on-Velocity (Trial no. 2)

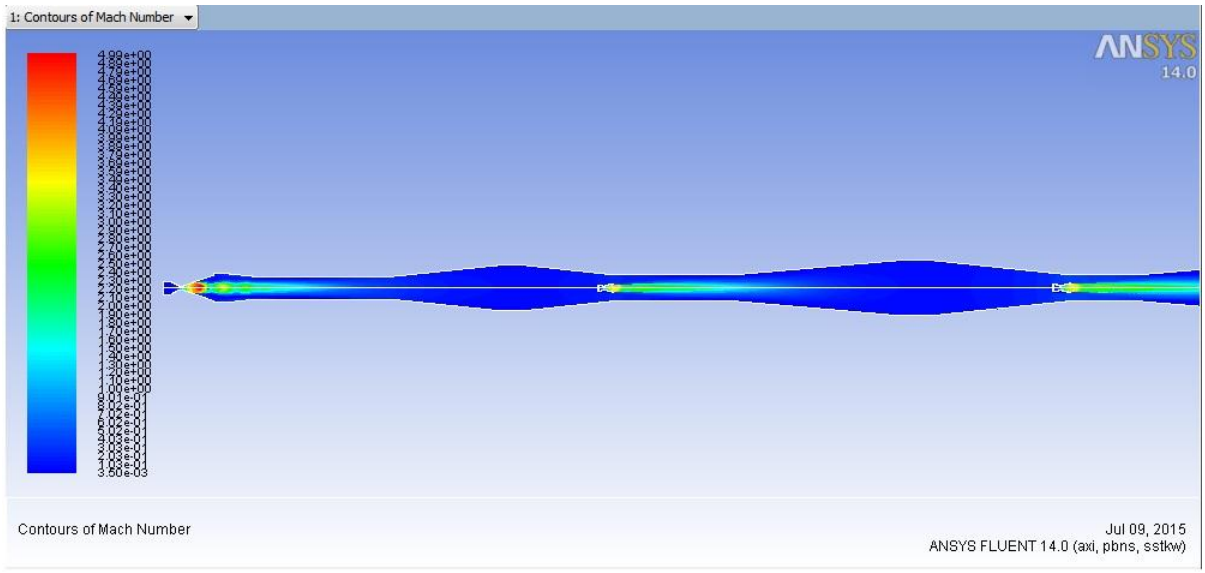

Fig. 31: All Nozzles on-Mach Number (Trial no. 2)

6.1.2.1. Results of Trial No. 2

From fig. 30 we see that the performance improved significantly but from the figure we still observe flow separation and full flow is still not achieved.

6.1.3. Trial No. 3

From the contour plots we can see the results improved with the second trial but flow separation still occurred. We further increased the flow rates. This time we increased the flow rate of the main nozzle to 0.03 kg/s and the flow rate of the second ejector nozzle to 0.055 kg/s.

Table 5: Boundary Conditions for Trial no. 3

Boundary	Boundary Condition	
	Type	**Measure**
Main nozzle inlet	Mass flow inlet	0.03 kg/s, 19.5 bar
1st Ejector inlet	Mass flow inlet	0.025 kg/s, 18 bar
2nd Ejector inlet	Mass flow inlet	0.055 kg/s, 24.2 bar
Exit	Pressure outlet	1 bar
Wall-zone	Wall	-
1st Ejector wall	Wall	-
2nd Ejector wall	Wall	-
Axis-line	Axis	-

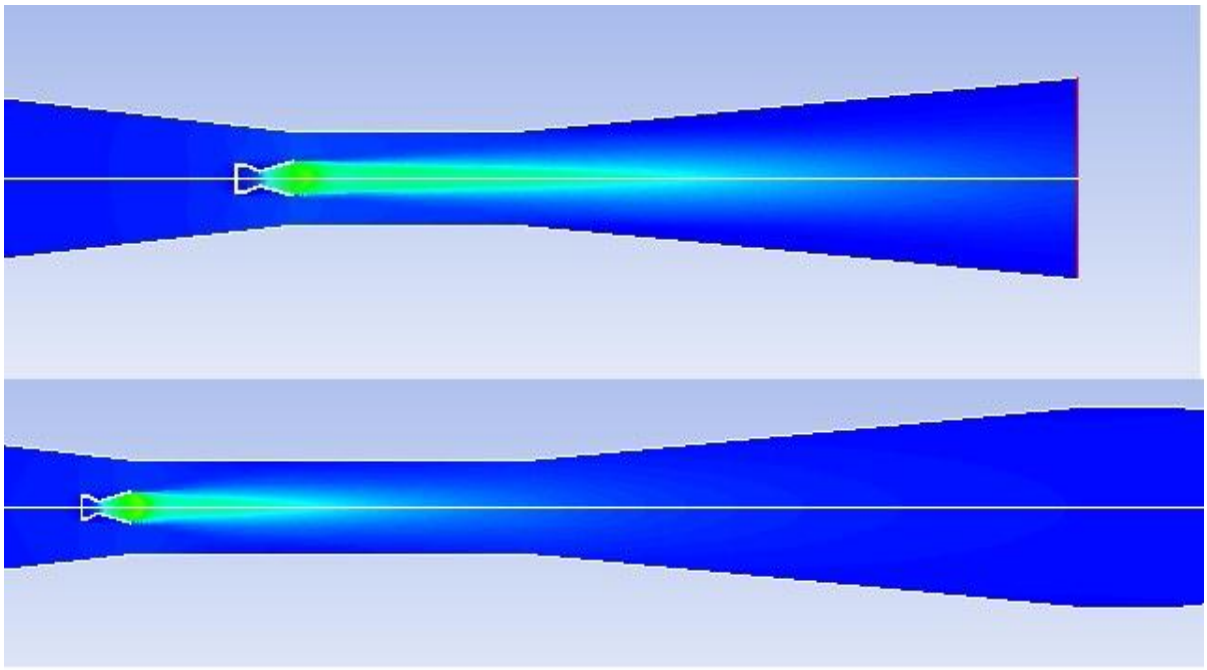

Fig. 32: Nozzles E1 and E2-Mach Number (Trial no. 3)

Fig. 31 shows that the ejector nozzles have been started. With the increased mass flow rate for the second ejector (0.055 kg/s) we see a marked improvement in the velocity and mach number of the second ejector (top ejector).

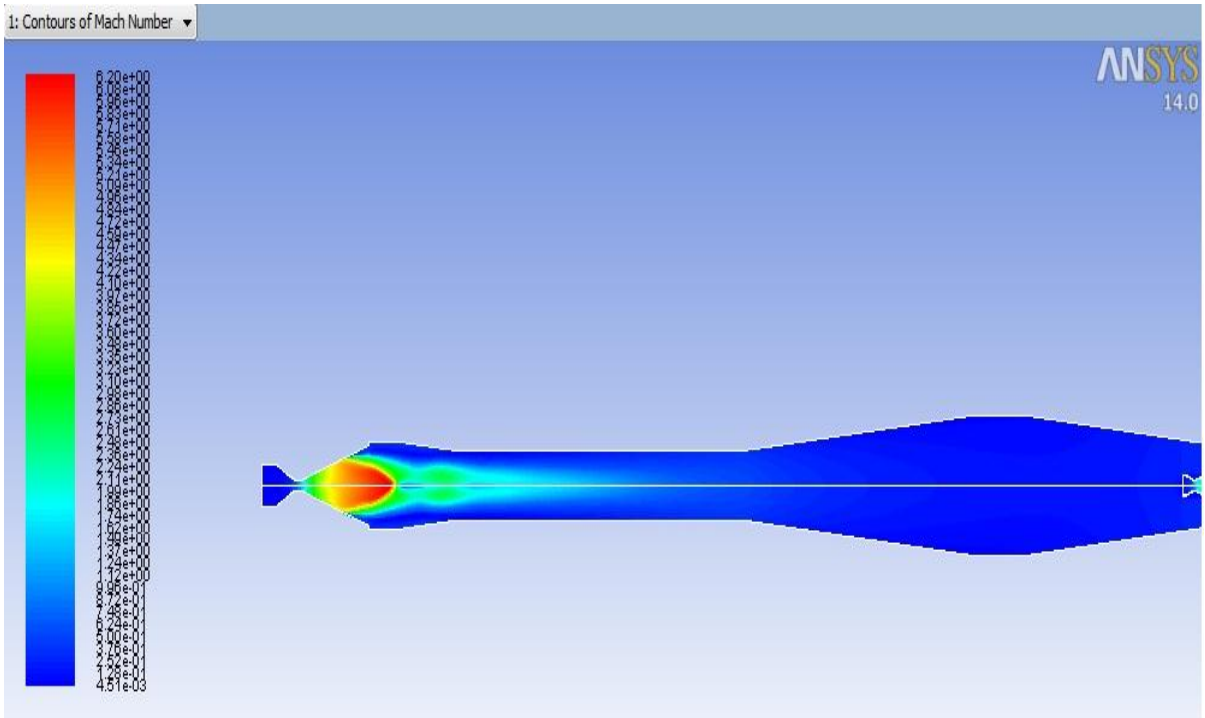

Fig. 33: Main Nozzle-Mach Number (Trial no. 3)

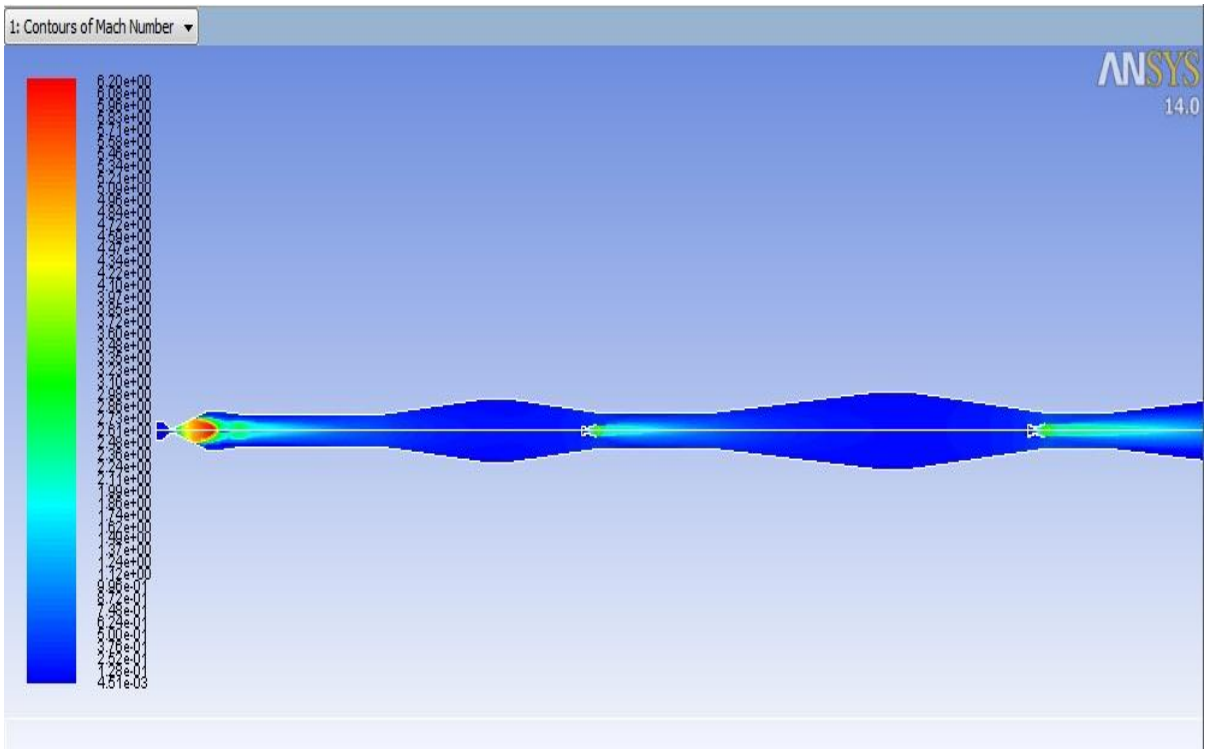

Fig. 34: All Nozzles on-Mach Number (Trial no. 3)

6.1.3.1. Results of Trial No. 3

From fig. 32 and fig. 33 we see that the performance improved but flow separation is still observed and even with these increased values we fail to achieve the desired full flow conditions.

6.1.3.2. Graphical Analysis (Pressure plot)

CFD-POST was used to make a graph of Pressure against Nozzle length at the axis. It is apparent that the pressure at the main nozzle exit is nearly zero (The main nozzle exit is at X=0.5 m). The two spikes along the way represent reservoir pressure of the ejectors.

Therefore we may conclude that the main nozzle has been evacuated to a value that is close to the desired vacuum level.

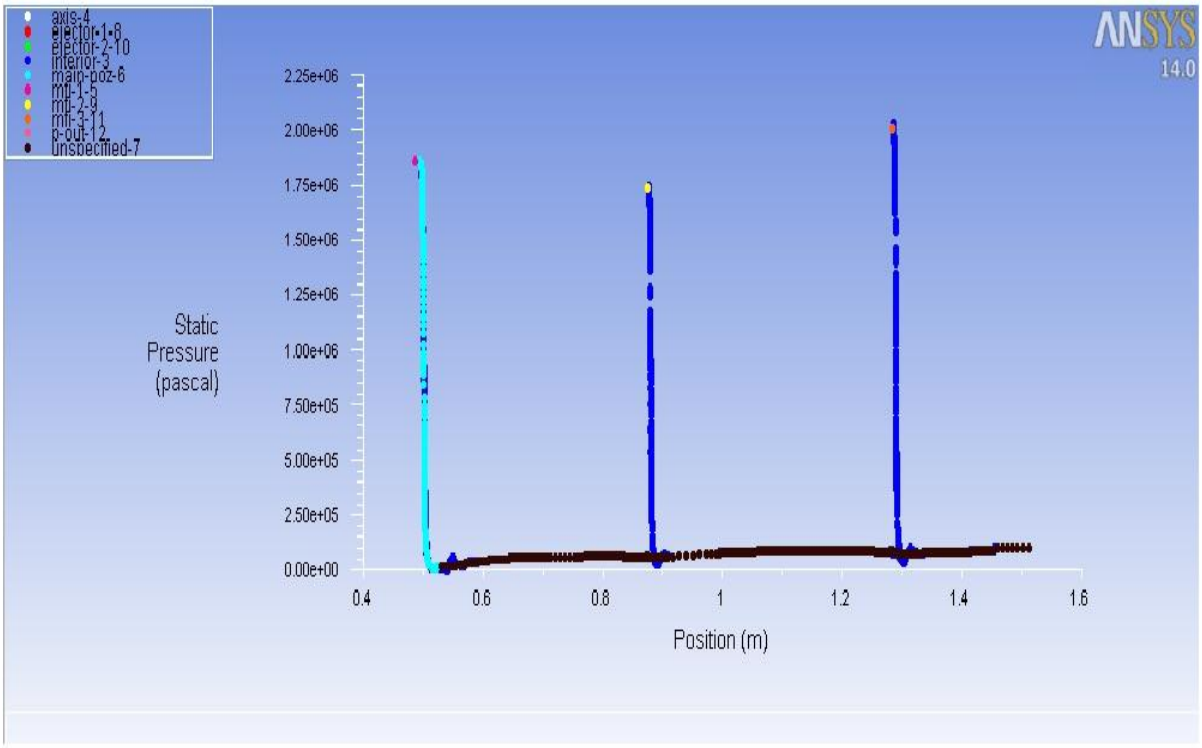

Fig. 35: Pressure vs Axial Length (Trial No. 3)

Fig. 34 shows the pressure plot of peak pressure against the axial length of the HAT Facility. The peaks in this plot define the pressures at the main nozzle, first ejector nozzle and the second ejector nozzle respectively. From this plot we can see that the pressure in the test chamber (i.e. the second throat exhaust diffuser) is around 10 mbar. This is very close to the desired vacuum level required in the chamber but is not sufficient to provide the vacuum level to achieve a full flow in the test chamber by the main nozzle.

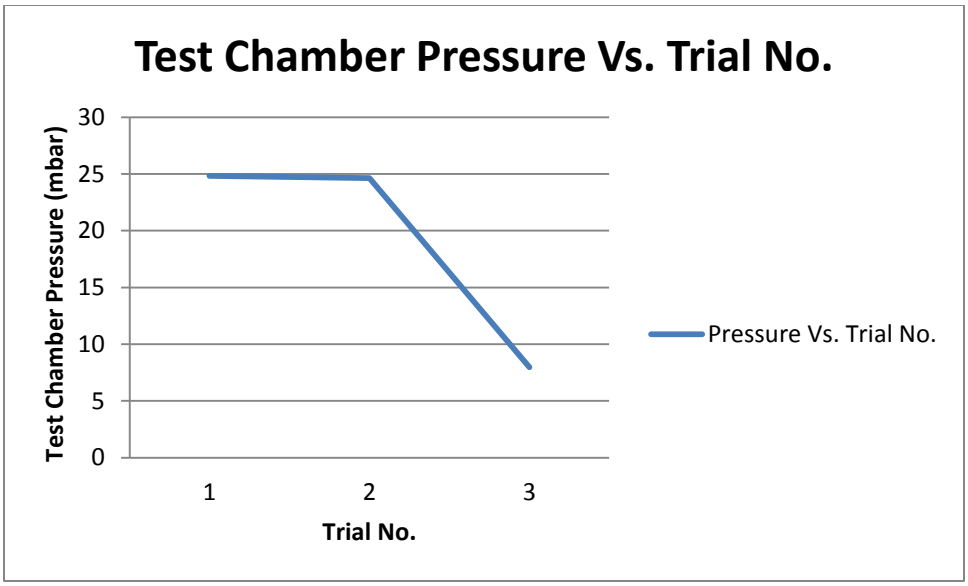

Fig. 36: Test Chamber Pressure Variation during the Trials

From the simulations we observed three main parameters whose values were critical for this study. The test chamber pressure, the maximum velocity attained by the thruster nozzle and the maximum Mach no. achieved by the thruster nozzle.

Fig, 35 shows the graph of the variation of the test chamber pressure when the boundary conditions were varied. The graph plot shows the minimum pressure reached in the test chamber and at trial no. 3 we see that we came closest to the desired 3 mbar chamber pressure. Yet it was not enough to get the desired flow conditions and eliminate flow separation.

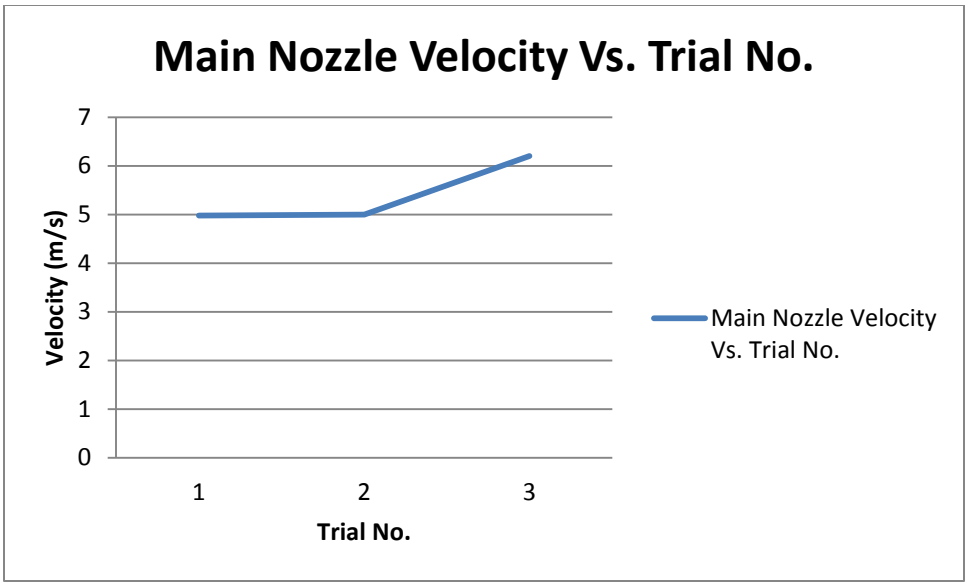

Fig. 37: Maximum Thruster Velocity during the Trials

Fig. 36 and 37 were plotted against the maximum flow velocity and maximum Mach no. attained by the main thruster nozzle, respectively. It can be seen from this graph that by changing the parameters we observed a steady increase in the flow velocity and hence the Mach no., which was as expected. But we failed to achieve the desired thrust values due to the occurrence of flow separation. Flow separation reduces the thrust and in turn decreases the efficiency of the nozzle.

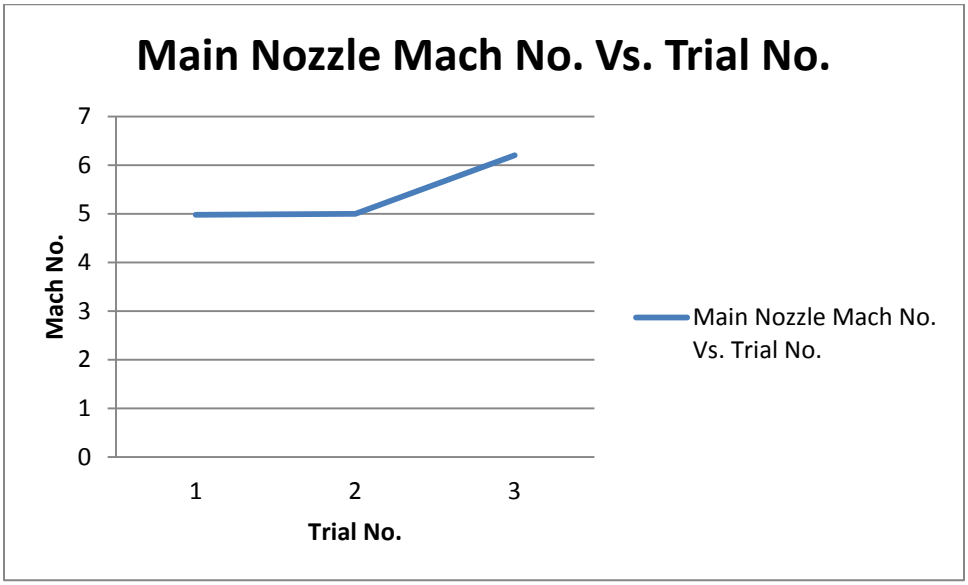

Fig. 38: Maximum Mach No. Reached during the Trials

6.2. Analysis

Looking at the above simulation trials we can observe that the chamber pressures were reduced to values very close to the required value (~3 mbar). However flow separation in the main thruster nozzle was still observed and the desired full flow was not achieved. Since additional simulations were run, just to check whether full flow could be achieved under a different set of parameters, we can safely say that none of those simulations bore any signs of a full flow. With this in mind a more logical answer seems to be the design of the main thruster nozzle or the design of the two-stage ejector system. The STED that was used was from the NASA study conducted by Massier et al [6]. This design was a tried and tested design with the design parameter equations provided to adapt to any nozzle.

Conclusion

Performance characteristics of a two-stage ejector system add-on have been simulated for producing the required high altitude conditions to test a large-area-ratio satellite thruster. It was shown, through CFD simulations that the main nozzle flow separated immediately without the aid of ejectors and therefore a two stage ejection system was necessary in combination with a second throat exhaust diffuser.

The numerical simulations show that the test facility was evacuated to a good extent at the provided design parameters but flow separation is still observed and the main thruster nozzle does not start at those conditions.

Main nozzle inlet	0.02 kg/s, 13 bar
1st Ejector inlet	0.025 kg/s, 18 bar
2nd Ejector inlet	0.045 kg/s, 19.8 bar

Even with alterations, shown in the table below, to the given conditions we observed that the main nozzle did not start.

Main nozzle inlet	0.03 kg/s, 19.5 bar
1st Ejector inlet	0.025 kg/s, 18 bar
2nd Ejector inlet	0.055 kg/s, 24.2 bar

From these observations we can safely conclude that even though the chamber was being evacuated to a good extent, we were not achieving the desired flow conditions. This result implies two things, either the design of the HAT needs to be optimized or the thruster nozzle itself needs to be redesigned.

The HAT is designed to simulate conditions found in the upper atmosphere or space i.e. near vacuum conditions. So according to this the HAT fulfills that criteria and provides a chamber pressure of ~3 mbar which was the necessary requirement. This leaves us with only one

remaining option and that is an inappropriate design of the thruster nozzle for the given design conditions. Factors affecting the efficiency of this nozzle could include the nozzle exit angle and the throat radius. Revisiting the design of the nozzle or the given initial conditions could improve results dramatically.

References

[1] ANSYS Fluent Theory Guide.

[2] ANSYS ICEM® Help.

[3] Menter, F. R. (1956). "Turbulence Modeling for Engineering Flows" ANSYS, Inc. Retrieved from http://simplorer.com/staticassets/ANSYS/staticassets/resourcelibrary/techbrief/tp-turbulence-modeling-for-engineering-flows.pdf

[4] Sung, Hong-Gye, Yeom, Hyo-Won, Yoon, Sangkyu, Kim, Seong-Jin, and Kim, Jingon. "Investigation of Rocket Exhaust Diffusers for Altitude Simulation" Journal of Propulsion and Power Vol. 26, No. 2, March–April 2010

[5] Watanawanavet, S. "CFD Optimization Study of High-Efficiency Jet Ejectors". Texas A&M University, May 2008.

[6] Massier, P. F., and Roschke, E. J. "Experimental Investigation of Exhaust Diffusers for Rocket Engines". Technical Release No. 34-59. Jet Propulsion Lab. May 5, 1960

[7] Keenan, J.H., Neumann, E.P., A Simple Air Ejector, J Applied Mechanics, Trans ASME 64, A75 - A81 (1942)

[8] Manikanda Kumaran R, Rajamani A, Raja Manohar D and Sundararajan T, Numerical Investigation on Second Throat Diffuser in High Altitude Test Facility of Satellite Thrusters, Proceedings of the 37th National & 4th International Conference on Fluid Mechanics and Fluid Power December 16-18, 2010, IIT Madras, Chennai, India.

[9] Ozair, Maryam, Qureshi, M. N., S. Zia-ur-Rehman, and Sultan, Q. "Numerical Investigation of a Supersonic Exhaust Diffuser for High Altitude Simulation", Institute of Space Technology, Karachi, Pakistan

[10] Ronan K. McGoverna, Kartik V. Bulusub, Mohammed A. Antarc and John H. Lienhard Vd, One-dimensional Model of an Optimal Ejector and Parametric Study of Ejector Efficiency, Proceedings OF ECOS 2012 - the 25TH International Conference on Efficiency, Cost, Optimization, Simulation and Environmental Impact of Energy Systems June 26-29, 2012, Perugia, Italy

[11] Chaqing Liao, B.S., Gas Ejector Modeling for Design and Analysis. (Dec 2008), Texas A&M University; Doctor of Philosophy.,

[12] A. Jeneev1, M. Jegesh David2, S. R. Balakrishnan, Second Throat Diffuser Inlet Configuration for Steering Engine, Department of Aeronautical Engineering, Nehru institute of engineering and technology, 2LPSC, Mahendragiri(June 2013)

[13] John D. Anderson Jr., Modern Compressible Flow With Historical Perspective, McGraw-Hill Series in Aeronautical and Aerospace Engineering

[14] Yinhai Zhu, Wenjian Cai , Changyun Wenb, Yanzhong Li , Numerical investigation of geometry parameters for design of high performance ejectors

[15] Kazuyasu Matsuo, Yoshiaki Miyazato, Heuy-Dong Kim, Shock train and pseudo-shock phenomena in internal gas flows, Progress in Aerospace Sciences 35 (1999)

[16] K. Annamalai, K. Visvanathan, V. Sriramulu, K.A. Bhaskaran, Evaluation of the performance of supersonic exhaust di€ user using scaled down models, Experimental Thermal and Fluid Science 17 (1998) 217-229

[17] DeFrate, L. A., and A. E. Hoerl, "Optimum Design of Ejectors Using Digital Computers," *Chem. Eng. Prog. Symp. Series*, **21** (1959).

[18] Fabri, J. and Siestrunck R., 1958, "Supersonic Air Ejectors," Advances in Appied Mechanics, Vol. **V**, pp. 1-34.

[19] Keenan, J.H. and Neumann, E.P., 1950, "An Investigation of Ejector Design by Analysis and Experiment," J. Applied Mechanics, Trans ASME, **72**, pp. 299-309.

List of Figures

List of Tables